EVALUATION OF A $^{90}Sr/^{90}Y$ BETA BEAM FLATTENING FILTER

by

Kevin Dean Stansbury

B.S., Kansas State University, 1982

A MASTER'S THESIS

submitted in partial fulfillment of the
requirements for the degree

MASTER OF SCIENCE

Department of Nuclear Engineering

KANSAS STATE UNIVERSITY

Manhattan, Kansas

1984

Approved by:

Major Professor

TABLE OF CONTENTS

LIST OF FIGURES

LIST OF TABLES

I. INTRODUCTION

In light of the restrictions placed on personnel exposure to beta radiation, means of measuring and monitoring beta radiation dose have been in a constant state of development and improvement for several years. But, in order to obtain accurate dose or dose rate information from beta radiation survey instruments and personnel dosimeters, the response of these devices to various fields of beta radiation must be known. Thus, standardized beta sources providing a uniform field of beta radiation must be employed for the calibration of such equipment.

Methods of calibration routinely used include exposure of devices to natural or depleted uranium slabs and exposure to point beta sources. Natural uranium slabs are reported[1] to provide a beta dose rate of 229 mrad hr^{-1} at a depth of 7 mg cm^{-2}, the depth for beta skin dose evaluation specified by the ANSI N13.11 standard.[2] A draft international standard,[3] ISO/DIS 6980, specifies the use of point beta radiation sources alone or in conjunction with beta beam flattening filters to provide uniform absorbed dose fields for instrument calibration. The beam flattening filter concept involves interposing a thin low atomic number absorber between a point source of beta radiation and the device to be evaluated. This filter is designed to provide the minimum beta particle attenuation necessary to give a uniform dose rate over a large area at a specified distance.

Experimental work was performed to evaluate a particular beta beam flattening filter designed for use with a combined $^{90}Sr/^{90}Y$ beta source. A plastic scintillator based spectrometer was utilized to measure the energy spectrum of beta particles attenuated by the filter as a result of

the spectrometer's low atomic number composition and its efficiency for detecting beta particles over the energy region of interest, below 2.3 MeV. Analysis of experimental pulse height distributions provided estimates of spectral shape changes and average beta particle energies that were used to determine estimates of the variation of absorbed dose over the calibration area. The beam flattener was studied for possible use in beta dosimetry experiments involving the accurate dosing of beta sensitive thermoluminescent dosimeters.

Beam flattening filters are used in Europe and Canada for the calibration of beta radiation survey instruments, but their use has been very limited in the United States. The Physikalisch-Technische Bundesanstalt currently provides calibrated beta source sets utilizing a beam flattener concept.[4] The dose rate at the calibration distance for a filter design similar to the one investigated in this research has been reported to vary less than ±5% across the area of uniform dose, a circle of 10 cm radius. Dose rate variation of less than ±1%, as estimated by a Geiger-Müller detector, has also been reported[5] for a similar filter. Most of these estimates were based upon measurements of count rates at several positions across the area, with the assumption that the average beta particle energy remained constant at all positions on the calibration area. Through measurements of spectra with a plastic scintillator based spectrometer, the validity of this assumption as well as the effectiveness of the beam flattening filter were tested.

Areas covered include a theoretical modeling of the beam flattening filter concept, the construction and calibration of the spectrometer, the evaluation of data collected with the spectrometer, and conclusions about the effectiveness of the particular beam flattening filter in providing a uniform dose over a large area.

II. THEORY

A. Attenuated Beta Particle Energy Distributions

In an effort to theoretically estimate the energy distribution of attenuated beta particles arriving at the calibration area in a beam flattening filter system, two methods are considered. The first approach involves a complicated geometrical treatment of the system, while the second provides a simple solution based on electron range-energy concepts. A beam flattening filter system can be modeled as presented in Fig. 2.1, where the beta source is assumed to be an uncollimated isotropic point source at a distance z from and along the axis of a detector with radius b. The energy distribution of beta particles reaching the detector is affected by the filter's composition and thickness, and by attenuation of particles in air. Filters used as beta particle beam flatteners are thin low atomic number materials (to minimize backscattering and bremsstrahlung production) of thickness t located at distance x from the detector and are parallel to the face of the detector.

As a result of the axial symmetry involved, the fraction of particles transmitted through the absorber and air which reach the detector may be evaluated by assuming the beta particles are "re-emitted" from points such as P in the filter. The difficulty in performing this calculation manifests itself in the form of the function used to describe the angular distribution of particles re-emitted from points in the filter. Because beta sources emit particles with a range of kinetic energies from zero to a maximum, various types of scattering occur in the filter including single scattering, multiple scattering, and diffusion. The model describing the angular distribution is dependent upon the type

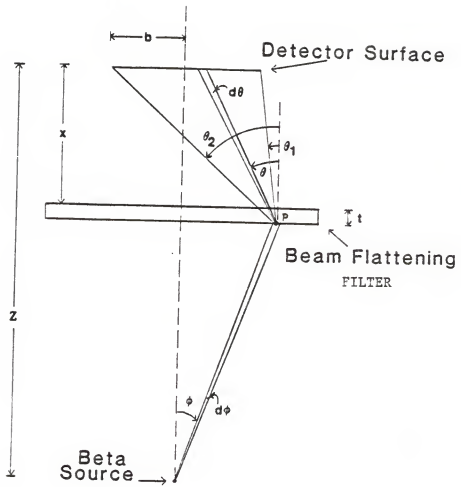

FIG. 2.1. Geometric arrangement of a beta beam flattening filter used in estimating the energy distribution of attenuated beta particles arriving at a detector of radius b.

of scattering involved and hence is a function of filter mass thickness and beta particle energy. Exponential attenuation of the particles in air and in source and detector windows must also be determined by choosing proper attenuation coefficients. Therefore, calculation of the energy distribution of particles reaching a detector entails numerical integration over the surface of the filter using various models[6] to approximate angular distributions over the proper energy ranges for the particular filter design investigated.

A less complicated approach to estimating the energy spectrum of beta particles arriving at the detector, after their attenuation in air, the beam flattening filter, and any other materials, is to use electron range-energy relationships. In the following discussion, the subscript i refers to beta particles incident upon an absorber while the subscript e refers to those particles emerging from the absorber which arrive at the detector. Assuming that beta particles of kinetic energy T_i, flux density energy distribution $\phi_i(T_i)$, and range $R_i(T_i)$ are normally incident on the absorber, particles which emerge have kinetic energy T_e, flux density energy distribution $\phi_e(T_e)$, and range $R_e(T_e)$. The ranges of incident and emergent beta particles are related as:

$$R_i(T_i) = R_e(T_e) + r, \tag{2.1}$$

where r represents the total absorber mass thickness which consists of the source window, air between the source and detector, the beam flattening filter, and the detector entrance window. The flux density energy spectrum of the emerging beta particles is given by[7]

$$\phi_e(T_e)dT_e = \phi_i(T_i)dT_i. \tag{2.2}$$

Because electron energy can be expressed as a function of electron range, and since the incident range can be calculated as a function of the emergent particle energy and absorber mass thickness, the following equation is obtained:

$$\phi_e(T_e) = \phi_i(T_i(R_i)) \frac{dT_i}{dT_e} = \phi_i(T_i(R_e(T_e)+r)) \frac{dR_e(T_e)/dT_e}{dR_i(T_i)/dT_i}. \qquad (2.3)$$

An electron range-energy relationship developed by Katz and Penfold[8] for aluminum was chosen for use in Eq. (2.3) to estimate $\phi_e(T_e)$:

$$R(T) = R_o T^n, \qquad (2.4)$$

where

$R(T)$ = beta particle range in g cm^{-2},

$R_o = 0.412$,

T = beta particle kinetic energy in MeV, and

$n = 1.265 - 0.0954 \ln T$.

This relationship is valid for electron energies ranging from 10 keV to 2.5 MeV. The expression for n is approximately independent of the attenuating medium, but R_o varies from one medium to another.[9] To simplify calculations involving Eq. (2.4), the value of R_o determined for aluminum was assumed to describe beta particle attenuation in all materials.

If the energy of incident beta particles is assumed to be known, the energy of particles emerging from the absorber may be evaluated by the following expression obtained from Eq. (2.4):

$$T_e = \exp\{6.63-3.2376\ [3.3067-\ln R(T_e)]^{\frac{1}{2}}\}, \qquad (2.5)$$

where $R(T_e)$ is determined by Eqs. (2.1) and (2.4) to be

$$R_e(T_e) = 0.412\ T_i^{n_i} - r. \tag{2.6}$$

The ratio of derivatives in Eq. (2.3) is then calculated using the following expression:

$$\frac{dR_e(T_e)/dT_e}{dR_i(T_i)/dT_i} = \frac{T_e^{(n_e-1)}\,[n_e-0.0954\ \ln T_e]}{T_i^{(n_i-1)}\,[n_i-0.0954\ \ln T_i]}. \tag{2.7}$$

This simple model neglects the effect of filter position on the calculated spectrum, and only simulates the attenuated spectrum along the axis of the beam flattening filter system. The flux density energy distribution of beta particles attenuated in a beam flattening filter may be estimated by combining Eqns. (2.3) and (2.7), provided that the flux density energy distribution of the incident beta particles is available. For a particular radionuclide, the incident beta spectrum can be obtained theoretically.

1. Beta particle energy distribution model

A model describing beta particle energy distributions is based upon the statistical nature of beta decay reactions. When a neutron (or proton) decays in the nucleus of an unstable atom, the negatron and anti-neutrino (or positron and neutrino) both share some of the energy, linear momentum, and angular momentum in the beta decay reaction. Through consideration of energy and momentum conservation, Fermi developed a quantum mechanical theory of beta decay in 1934,[10] which included the statistical probability of energy division between the negatron and anti-neutrino (the magnitude of the recoil kinetic energy of

the nucleus is negligible). Thus, the probability that a beta particle is emitted with total relativistic energy between W and W+dW is described by[11]

$$N(W)dW = (g^2/2\pi^3)F(\pm Z,W)PW(W_o-W)^2 S_n(W)dW, \quad \text{for } e^{\mp}, \tag{2.8}$$

where

g^2 = a coupling constant

$F(\pm Z,W)$ = electron density ratio or Fermi function,

$$P = (W^2-1)^{\frac{1}{2}} = \text{beta particle momentum,} \tag{2.9}$$

$S_n(W)$ = shape factor,

$$W = (E_k/m_o c^2) + 1, \tag{2.10}$$

= total relativistic energy of a beta particle with kinetic energy E_k, in units of electron rest mass energy, $m_o c^2$, and

W_o = maximum relativistic energy with which the beta particle is emitted.

The following model, used in determining the electron density ratio $F(\pm Z,W)$, was obtained from a solution of the relativistic (Dirac) equation for an electron in the electrostatic field of a nucleus:[12]

$$F(\pm Z,W) = \frac{4(1+\frac{s}{2})}{|\Gamma(3+2s)|^2}\left(\frac{2R}{\lambda_c}\right)^{2s} e^{\pi y}\,(W^2-1)^s\,|\Gamma(1+s+iy)|^2, \tag{2.11}$$

where

α = fine structure constant ($\sim 1/137$),

$$y = \pm Z\alpha W/P, \text{ for } e^{\mp}, \tag{2.12}$$

$$s = [1-(\alpha Z)^2]^{\frac{1}{2}} - 1, \tag{2.13}$$

λ_c = rationalized Compton wavelength of an electron ($\sim 386 \times 10^{-13}$ cm),

$$R = \text{nuclear radius} = (1.123\ A^{1/3} - 0.941\ A^{-1/3}) \times 10^{-13}\ \text{cm}, \tag{2.14}$$

A = atomic mass number, and

Z = atomic number of the daughter isotope.

The shape factor $S_n(W)$ describes changes in the probability distribution due to the nature of beta particle transitions. Allowed transitions have a statistical shape and thus have a shape factor $S_0(W) = 1$. The shapes of beta particle energy distributions from forbidden transitions are influenced by changes in the spin and angular momentum of particles. Several different models have been developed for the calculation of these shape factors, and the expressions selected in this research for first and second forbidden unique transitions are

$$S_1(W) = P^2 + (W_0-W)^2, \text{ and} \tag{2.15}$$

$$S_2(W) = P^4 + (W_0-W)^4 + \frac{10}{3} P^2 (W_0-W)^2. \tag{2.16}$$

Empirical results have shown that spectra from non-unique first forbidden beta decay possess a shape similar to that exhibited by allowed transitions, and non-unique second forbidden decay results in a beta particle energy distribution shape similar to the unique first forbidden transition.[13]

The Bethe-Bacher approximation to $|\Gamma(1+s+iy)|^2$ was substituted into the expression for $F(\pm Z,W)$ in Eq. (2.11),

$$|\Gamma(1+s+iy)|^2 \cong |\Gamma(1+iy)|^2 (y^2+\tfrac{1}{4})^s \tag{2.17}$$

$$= \left(\frac{\pi y}{\sinh \pi y}\right) [(\alpha^2 Z^2+\tfrac{1}{4})W^2 - \tfrac{1}{4}]^s. \tag{2.18}$$

The expression for the Fermi function was also modified to correct low energy portions of the calculated beta spectra from heavy elements

for the screening effect of atomic electrons. The following expression replaced $F(\pm Z,W)$ in Eq. (2.8):

$$F(\pm Z, W\mp V_o) \left(\frac{(W\mp V_o)^2 - 1}{P^2}\right)^{\frac{1}{2}} \left(\frac{W\mp V_o}{W}\right), \text{ for } e^{\mp}. \tag{2.19}$$

The quantity V_o represents a shift in potential energy near the nucleus arising from screening and is estimated by

$$V_o = 1.13\ \alpha^2\ Z^{4/3}. \tag{2.20}$$

Another manner in which beta spectra may be represented is the Kurie plot. The plot is constructed by rearranging Eq. (2.8) to obtain an expression that is linear with respect to the parameter W,

$$\left\{\frac{N(W)}{(g^2/2\pi^3)F(\pm Z,W)PW\ S_n(W)}\right\}^{\frac{1}{2}} = W_o - W. \tag{2.21}$$

Thus a Kurie plot presents the beta spectrum as a straight line which intercepts the W-axis at W_0. The Kurie plot is used to estimate endpoints of measured beta spectra and to observe distortions in measured beta pulse height distributions which result in the presence of non-linear regions in the plots.

a. Relativistic model comparison. When the model for calculating theoretical beta spectra was selected, average beta energy estimates and spectrum shapes were compared to other theoretical and experimental results. Table 2.1 presents average energies of various beta spectra determined by several authors. The relativistic model chosen for this research, involving the evaluation of a beta beam flattening filter, predicted average energies which were generally in agreement with other

TABLE 2.1. Comparison of average beta energies for several beta emitters reported by various authors.

Isotope	A	Z	Average Beta Energy				
			Table of Isotopes[a] (MeV)	Berger[b] (MeV)	Mantel[c] (MeV)	Cross[d] (MeV)	Relativistic Model (MeV)
C	14	6	0.0467	0.0493	0.0493	0.0495	0.0492
Pm	147	61	0.0605	0.0621	...	0.0620	0.0622
Ca	45	20	...	0.0773	0.0762	0.0772	0.0781
W	185	74	0.144	...	...	...	0.118
Sr	90	38	...	0.1963	0.1961	0.196	0.199
Tl	204	81	...	0.2433	...	0.238	0.235
Cl	36	17	...	0.2525	0.3213	0.312	0.251
P	32	15	0.694	0.6950	0.6929	0.695	0.694
Y	90	39	...	0.9367	0.9335	0.934	0.930

[a]From Table of Isotopes, 7th ed., John Wiley and Sons (1978).

[b]From M. J. Berger, J. Nucl. Med., 12, Supplement No. 5 (1970).

[c]From J. Mantel, Int. J. of Appl. Rad. and Isot., 23 (1972).

[d]From W.G. Cross, H. Ing, and N. Freedman, presented at the International Beta Dosimetry Symposium, Washington D.C., 1983 (unpublished).

estimates. Some actual spectrum comparisons were made with theoretical data from Cross[14] and are presented in Figs. 2.2 - 2.4 for ^{36}Cl, ^{147}Pm, and $^{90}Sr/^{90}Y$, respectively.

Spectra calculated by the relativistic model for isotopes with high atomic numbers exhibited the greatest deviation from the spectra calculated by Cross in the low energy region. The difference may be related to over idealization of the nucleus as a point charge[15] and the presence of the screening correction in the calculation of Fermi function values. The ^{36}Cl spectrum shape determined by the relativistic model differs from the Cross model and predicts a significantly different average beta energy. The difference may be attributed to the fact that the energy spectrum has a second forbidden non-unique shape, and Cross used an experimentally determined shape factor. An allowed shape was assumed with the relativistic model because of its agreement with experimentally measured ^{36}Cl spectra. Extreme divergence between the two models in the low energy region is exhibited by the ^{147}Pm beta particle energy distribution due to the high atomic number of the isotope. The two models appear to be very similar in the case of the combined $^{90}Sr/^{90}Y$ spectrum.

B. Comparison Between Theoretical and Measured Attenuated Spectra

When considering the comparison of a measured $^{90}Sr/^{90}Y$ beta particle energy spectrum attenuated by a beam flattening filter to an absorption corrected theoretical $^{90}Sr/^{90}Y$ distribution, there was an interest in determining how effectively the theoretical absorption correction modeled actual measured data. Experimental results of an absorption study[16] were compared with calculated ^{36}Cl, ^{185}W, and $^{90}Sr/^{90}Y$

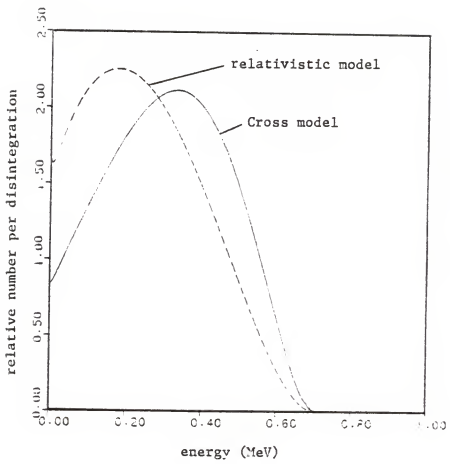

FIG. 2.2. Comparison of the relativistic model to a model developed by Cross for the ^{36}Cl beta particle energy distribution.

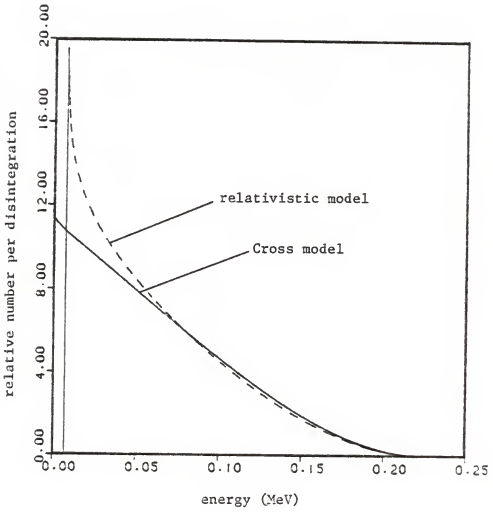

FIG. 2.3. Comparison of the relativistic model to a model developed by Cross for the ^{147}Pm beta particle energy distribution.

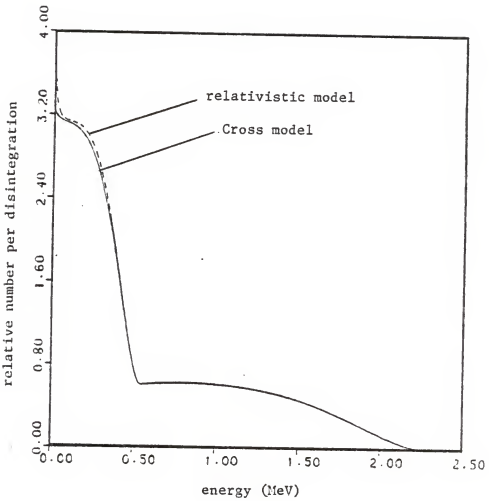

FIG. 2.4. Comparison of the relativistic model to a model developed by Cross for the combined $^{90}Sr/^{90}Y$ beta particle energy distribution.

beta spectra to which the simulated absorption correction had been applied. A computer code (ABSCOR) was developed to calculate incident and attenuated spectra, and provide estimates of spectrum areas, average beta particle energies, and spectrum energy endpoints.

Theoretical unattenuated spectra and spectra of beta particles penetrating several absorbers of various mass thicknesses were calculated. Assuming that the relativistic beta particle energy distribution model described in Section 2.A.1 was related to the flux density energy spectrum of unattenuated beta particles, the relationship described by Eq. (2.3) was used to calculate attenuated spectra. In Eq. (2.3), $\phi_i(T_i)$ represents the flux density energy spectrum of beta particles emitted from the source and incident upon the absorber, while $\phi_e(T_e)$ represents the flux density energy spectrum at the surface of the detector. An electron range-energy relationship used to calculate the absorption corrected spectra was that developed by Katz and Penfold, given in Eq. (2.4), which defines the range in g cm^{-2} of a beta particle with kinetic energy T in MeV. Another model was tested for ^{185}W and was developed by Flammersfeld in 1946:

$$R(T) = \frac{(22.4T^2+1)^{\frac{1}{2}} - 1}{9.1}. \qquad (2.22)$$

The absorption correction model did not account for variations in spectral shapes due to resolution broadening in the spectrometer and backscattering of beta particles.

All measured spectra were collected with a 10.2 mm thick BC-400 plastic scintillator based spectrometer under fixed source-detector geometry conditions. Absorbers interposed between the source and

detector consisted of thin polyester sheets and the total absorber was composed of the source window, aluminum detector window of 2.43 mg cm^{-2}, and the polyester sheets (a small air thickness was assumed to have negligible mass thickness).

Figure 2.5 displays measured ^{36}Cl spectra for increasing absorber thicknesses from 2.9 to 88.3 mg cm^{-2}, while Fig. 2.6 shows calculated ^{36}Cl spectra for increasing absorber thicknesses from 0 to 150 mg cm^{-2}. The percent change in spectrum area for increasing absorber thickness relative to the area obtained at a thickness of 2.93 mg cm^{-2} is illustrated in Fig. 2.7 and the results from measured spectra suggest that a higher degree of attenuation takes place in the measured data than the absorption correction model predicts. However, both follow the same exponential trend. Figure 2.8 presents the variation of spectrum average energy with increasing absorber thickness for ^{36}Cl. The model appears to approximate the trend of the measured data, with an initial increase in average energy followed by a slow decrease with increasing absorber mass thickness. Differences in the areas and average energies between measured data and the predictions are attributed to backscattering in the ^{36}Cl source (thick aluminum backing), the type of absorber used, the energy calibration of the spectrometer, air scattering, and the possible inadequacy of the theoretical model used to define the unattenuated beta particle energy distribution for ^{36}Cl.

Results shown in Figs. 2.9 and 2.10 illustrate measured and estimated spectrum shape changes for ^{185}W with increasing absorber mass thickness. Again, the model predicts less severe attenuation of the beta particles than the measured data indicate (see Fig. 2.11). The variation of average energy with increasing absorber thickness, demonstrated in

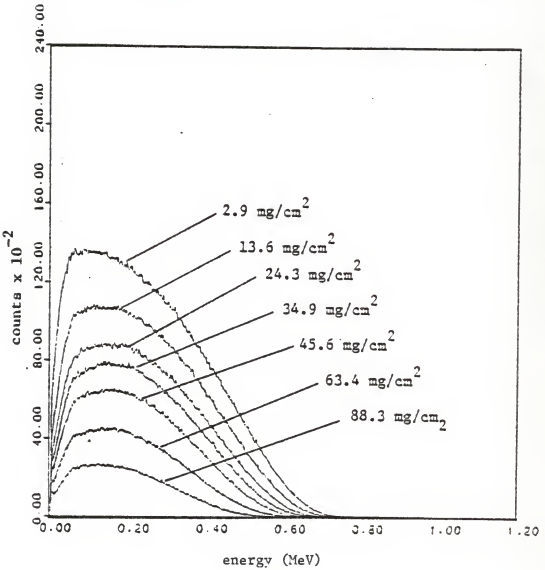

FIG. 2.5. Beta particle energy distribution of ^{36}Cl as a function of increasing absorber thickness. Spectra were collected with a 10.2 mm BC-400 plastic scintillator based spectrometer (from reference 16).

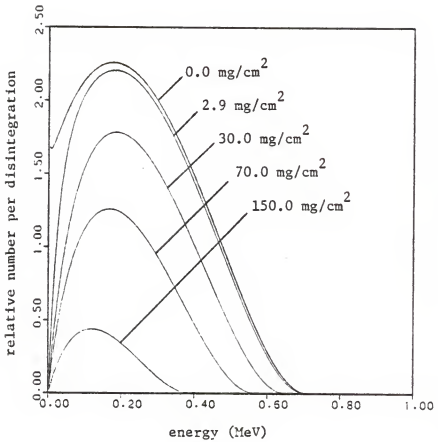

FIG. 2.6. Calculated beta particle energy distribution for ^{36}Cl as a function of increasing absorber thickness. Distributions were estimated by the relativistic model with an absorption correction.

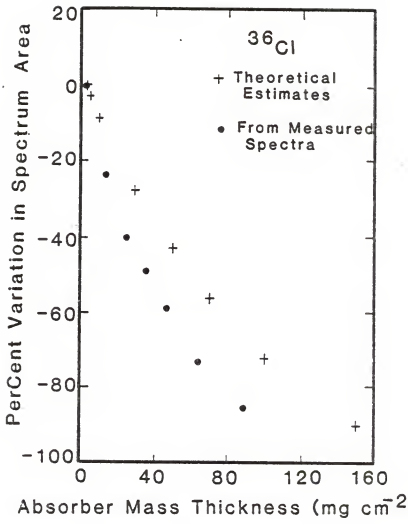

FIG. 2.7. Comparison of theoretically estimated changes in the area of the ^{36}Cl beta particle energy distribution to results from measured data for increasing absorber thickness. Percent variation is based upon the values obtained at a total absorber mass thickness of 2.9 mg cm^{-2}.

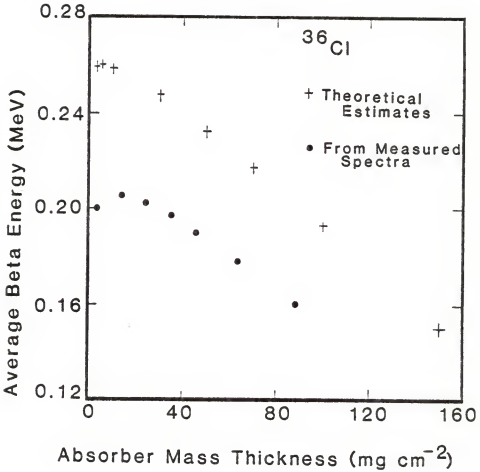

FIG. 2.8. Comparison of theoretically estimated changes in the average energy of the ^{36}Cl beta particle energy distribution to results from measured data for increasing absorber mass thickness.

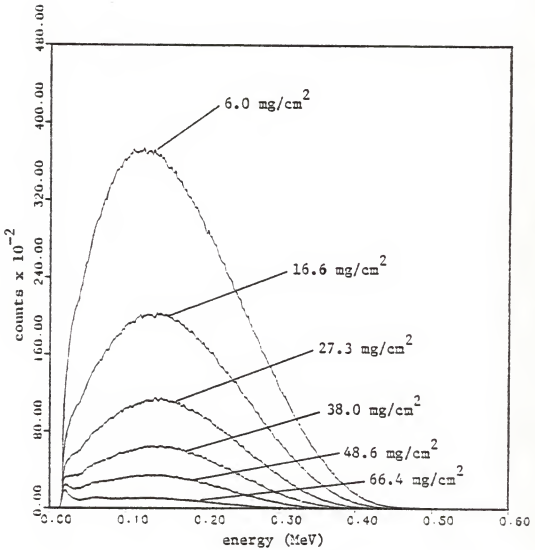

FIG. 2.9. Beta particle energy distribution for ^{185}W as a function of increasing absorber thickness. Spectra were collected with a 10.2 mm BC-400 plastic scintillator based spectrometer (from reference 16).

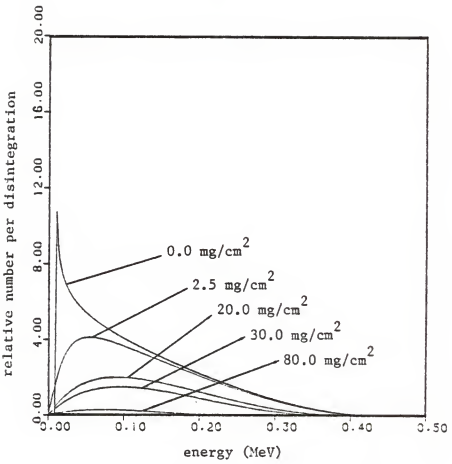

FIG. 2.10. Calculated beta particle energy distribution for ^{185}W as a function of increasing absorber thickness. Distributions were estimated by the relativistic model with an absorption correction.

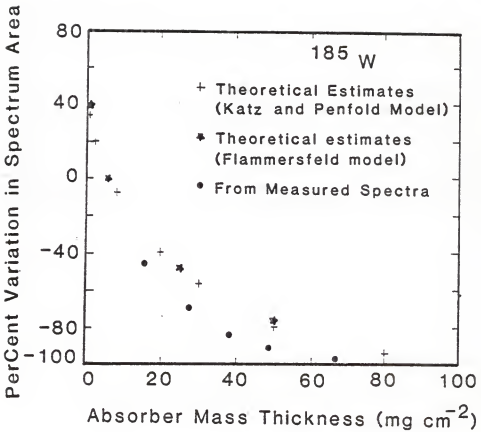

FIG. 2.11. Comparison of theoretically estimated changes in the area of the ^{185}W beta particle energy distribution to results from measured data for increasing absorber thickness. Percent variation is based upon the values obtained at a total absorber mass thickness of 6.0 mg cm^{-2}.

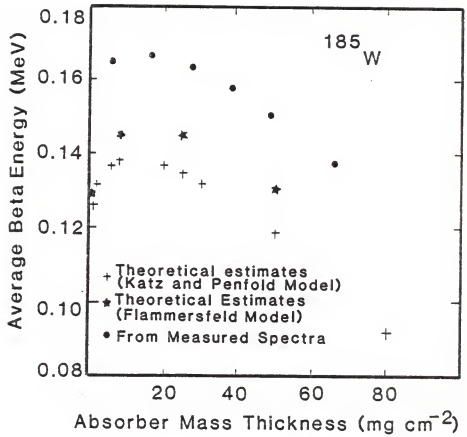

FIG. 2.12. Comparison of theoretically estimated changes in the average energy of the ^{185}W beta particle energy distribution to results from measured data for increasing absorber mass thickness.

Fig. 2.12, indicates that the model underestimates the average energy of the measured data, but it does seem to follow the same trend. Major differences are attributed to the inadequacy of the theoretical model used to determine the unattenuated ^{185}W spectrum. Results from the simulated absorption corrected data calculated with the Flammersfeld range-energy relationship appear to more closely approximate the measured results than those calculated with the Katz and Penfold relationship for ^{185}W beta particle energy distributions.

Finally, an attempt was made to model spectral shape changes of the combined $^{90}Sr/^{90}Y$ beta spectrum for increasing absorber thickness. Examples of measured and calculated spectra are provided in Figs. 2.13 and 2.14. The percent variation in integral counts with increasing absorber mass thickness (shown in Fig. 2.15) again suggests that the model underestimates the degree of attenuation of beta particles in the absorbers. Similar changes in average beta energy are also predicted by the model (see Fig. 2.16). The results from measured data imply that the lower energy beta particles from ^{90}Sr are almost completely attenuated in approximately 110 mg cm^{-2} of absorber, while the model predicts a value near 150 mg cm^{-2}.

Appendix A presents the effects of the absorption correction on calculated Kurie plots of beta particle energy distributions for ^{36}Cl, ^{185}W, and $^{90}Sr/^{90}Y$.

C. Prediction of the Attenuated Spectral Shape.

Using the theoretical model presented in Section 2.A in conjunction with the absorption correction model, the energy distribution of beta particles attenuated by the beam flattening filter under investigation

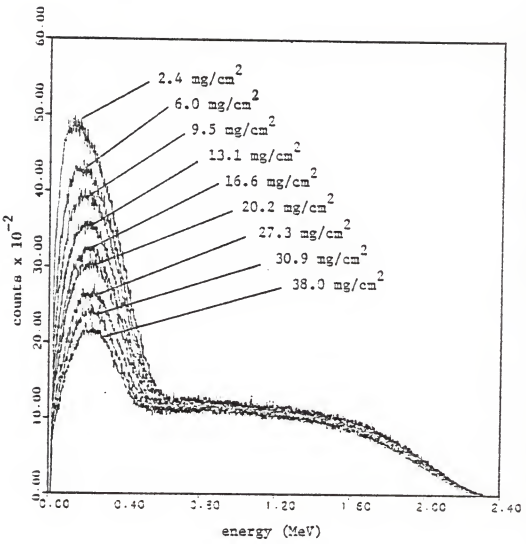

FIG. 2.13. Combined beta particle energy distribution for $^{90}Sr/^{90}Y$ as a function of increasing absorber thickness. Spectra were collected with a 10.2 mm BC-400 plastic scintillator based spectrometer (from reference 16).

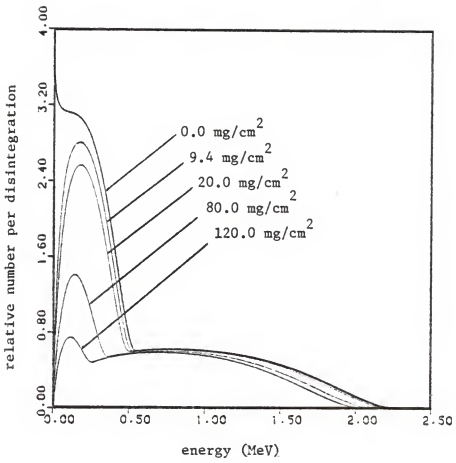

FIG. 2.14. Calculated beta particle energy distribution for $^{90}Sr/^{90}Y$ as a function of increasing absorber thickness. Distributions were estimated by the relativistic model with an absorption correction.

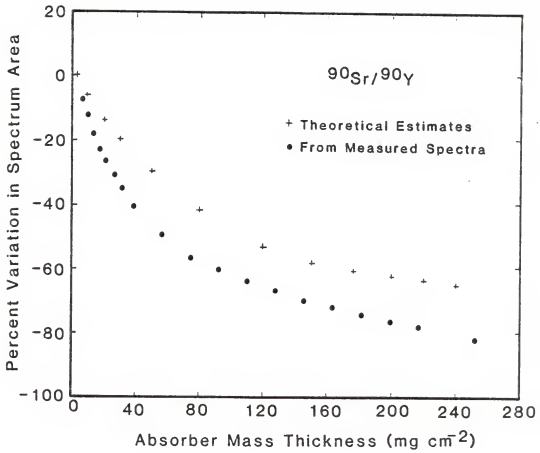

FIG. 2.15. Comparison of theoretically estimated changes in the area of the combined $^{90}Sr/^{90}Y$ beta particle energy distribution to results from measured data for increasing absorber thickness. Percent variation is based upon the values obtained at a total absorber mass thickness of 3.3 mg cm^{-2}.

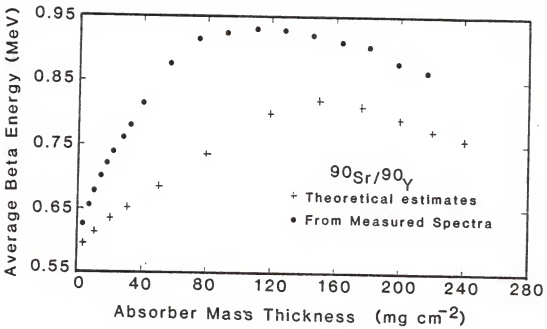

FIG. 2.16. Comparison of theoretically estimated changes in the average energy of the combined $^{90}Sr/^{90}Y$ beta particle energy distribution to results from measured data for increasing absorber thickness.

was estimated and is presented in Fig. 2.17. A theoretical $^{90}Sr/^{90}Y$ spectrum with no absorption correction is also provided. Because the total mass thickness of the absorber (including source window, air, filter, and detector entrance windows) was estimated to be 175.8 mg cm^{-2} along the central axis of the filter system, the contribution of the ^{90}Sr beta particles to the attenuated spectrum was almost completely eliminated. Thus, the shape was primarily described by attenuated ^{90}Y beta particles with an endpoint energy of 1.959 MeV. The calculated average energy of the attenuated spectrum was 0.8085 MeV, compared to 0.5645 MeV obtained from the unattenuated spectrum. The measured average energy of attenuated beta particles was expected to be near the predicted value. But, a difference was anticipated as a result of the absorption model assumptions and due to the results of measured data in Section 2.B., which indicated an average energy near 0.9 MeV. Figure 2.18 illustrates the theoretical Kurie plots of the spectra in Fig. 2.17.

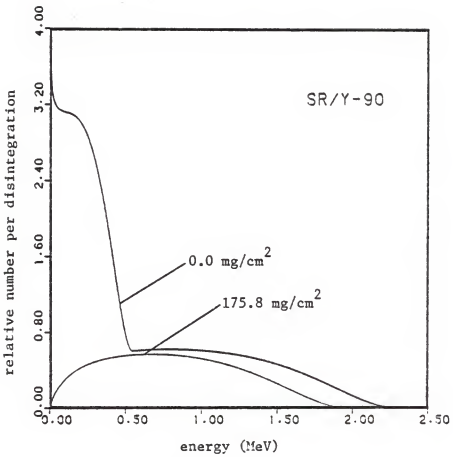

FIG. 2.17. Comparison of the theoretical shape of the combined $^{90}Sr/^{90}Y$ beta particle energy distribution to the theoretical shape corrected for particle attenuation in a total absorber mass thickness of 175.8 mg cm^{-2}. Distributions were estimated by the relativistic model with an absorption correction.

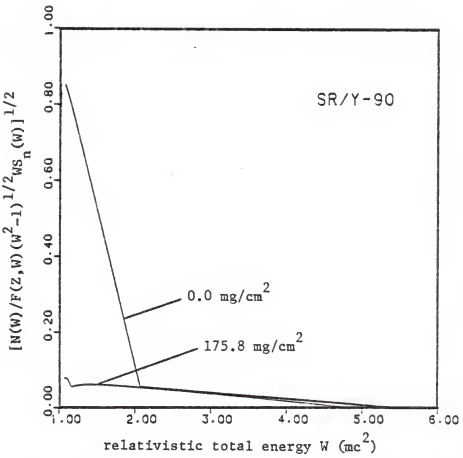

FIG. 2.18. Comparison of the theoretical Kurie plot for the combined $^{90}Sr/^{90}Y$ beta particle energy distribution to the Kurie plot corrected for particle attenuation in a total absorber mass thickness of 175.8 mg cm^{-2}. Plots were estimated by the relativistic model with an absorption correction.

III. METHODS AND MATERIALS

A. Beam Flattening Filter Description

The beam flattening filter designed for use with a $^{90}Sr/^{90}Y$ beta source consisted of 3 concentric discs of polyester, each with a mass thickness of approximately 25 mg cm^{-2} and radii of 2 cm, 3 cm, and 5 cm. Filter design was dependent upon parameters such as the energies of beta particles emitted from the source, the distance between source and calibration plane, and the distance from source to filter. For the filter described, the source to filter distance was 10 cm and the source to calibration plane distance was 40 cm. The arrangement was designed to produce a uniform dose rate over a large area on the calibration plane. The optimum filter configuration with a source-to-calibration plane distance of 30 cm was estimated to provide a uniform dose over an area 20 cm in diameter, but count rate limitations on the BC-400 plastic scintillator based spectrometer restricted the investigation to source to calibration plane distances greater than or equal to 40 cm. In actual application, the dose rate at the calibration plane is changed by varying the source strength, not by altering the geometry of the system. The beam flattening filter set up is illustrated in Fig. 3.1.

B. The Beta Spectrometer

1. Plastic scintillator detector characteristics

A BC-400 plastic scintillator detector was chosen to measure the energy spectrum of beta particles attenuated by the beam flattening filter. This type of detector was selected as a result of its collection efficiency for electrons and because beta pulse height distributions

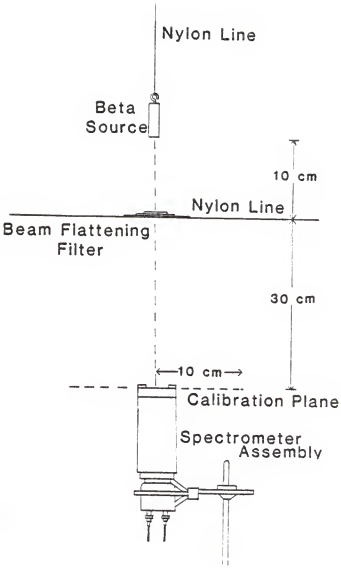

FIG. 3.1. Experimental arrangement used in the evaluation of a $^{90}Sr/^{90}Y$ beta beam flattening filter with a plastic scintillator based spectrometer.

measured with this detector exhibited relatively low distortion, allowing evaluation of spectral shape changes and estimation of beta endpoint and average energies.

a. Collection efficiency. The BC-400 scintillator was shaped in the form of a right circular cylinder, 50.8 mm in diameter and 10.2 mm thick. This scintillator was of sufficient mass thickness (1049 mg cm^{-2}) to completely attenuate beta particles with energies up to 2.3 MeV. The detector was also fitted with a light-tight 9 μm aluminum foil entrance window. All beta particles with energies below approximately 40 keV were attenuated in this foil window, which had a mass thickness of 2.43 mg cm^{-2}. Thus, the BC-400 plastic scintillator based spectrometer was nearly 100% efficient for detecting beta particles with energies between 40 keV and 2.3 MeV.

b. Distortive effects. The plastic scintillator's major distortive effects are related to its low energy resolution in response to monoenergetic electrons and due to the incomplete absorption of electron energy within the scintillator. If scintillator detectors exhibited perfect energy resolution, the response of the detector to monoenergetic radiation would be represented by a delta function. But, as a consequence of resolution broadening in the detector and associated electronics, the response to monoenergetic electrons which are completely absorbed in the scintillator may be closely approximated by a Gaussian distribution. Resolution broadening occurs as a result of the statistical nature of the counting process and the collection of photons by the photomultiplier tube. Thus, the extent of broadening is related to the particular spectrometer used to record data and upon the energies

of the incident radiation. The monoenergetic electron response may be further altered by incomplete absorption of electron energy due to backscatter out of the detector, by detection of electrons which have been degraded in energy before reaching the scintillator, and by detection of electrons which lose a fraction of their energy through generation of bremsstrahlung photons which escape the scintillator. These effects result in a skewing of the Gaussian line shape with a tail extending toward lower energies. Because of the low Z composition of plastic scintillators, the backscatter effect on line shape is negligible, and the probability of bremsstrahling photon production is small. Thus, the major distortion in Gaussian line shape is produced through detection of electrons which have lost energy through backscattering and attenuation in the source material and encapsulation. Electrons also suffer energy losses in any air between source and detector, and in the detector window.

c. Beta particle response. Beta spectra measured with the BC-400 plastic scintillator based spectrometer were subject to the distortions described in the previous section. Resolution broadening inherent to the spectrometer created distortions near the high energy regions of measured pulse height distributions, causing the spectra to extend beyond true endpoints. Limited studies in which resolution broadening was mathematically simulated with a modified Gaussian model in certain theoretical beta spectra suggested that broadening induces only slight distortions in the spectra near beta endpoints and has little effect on the estimation of average spectrum energies (see Appendix B). Scattering of beta particles in source material, source encapsulation, and in the

detector window produced distortion in the low energy region of measured distributions and affected average beta energy estimates, but had little effect on beta endpoint energy calculations.

Plastic scintillators are reported to produce light pulses which are linearly proportional to electron energy deposited in the detector, for deposited energy greater than 125 keV.[17] The energy expended in the scintillator is dependent upon incident particle energy, and the mass thicknesses of the entrance window and the scintillator. Below approximately 125 keV, light output is very sensitive to the rate of electron energy dissipation along the particle's path, and output is not a linear function of electron energy.

An example of beta particle response of the 10.2 mm BC-400 plastic scintillator based spectrometer is illustrated by Fig. 3.2 in which a measured $^{90}Sr/^{90}Y$ beta particle pulse height distribution is presented.

d. Gamma photon response. As a consequence of the plastic scintillator's low Z composition, monoenergetic gamma rays with energies between 100 keV and 3 MeV interacting in the detector primarily undergo Compton scattering, producing a pulse height distribution of recoil electron energy related to the Compton scattering cross section. These Compton recoil electrons are scattered with kinetic energies from zero to a maximum. But, the maximum recoil electron energy position is not well defined and lies somewhere along the measured Compton edge because of the possibility of Compton scattered electron escape with partial energy deposition in the detector and due to the inherent energy resolution of the spectrometer. This position is also influenced by the probability of multiple scattering in the scintillator, which is dependent upon photon

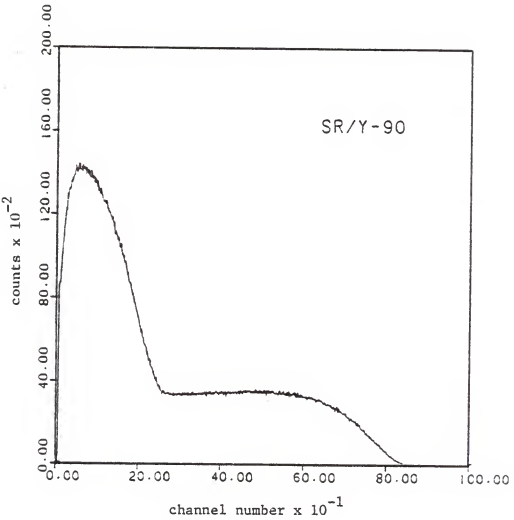

FIG. 3.2. Pulse height distribution of beta particles emitted from a $^{90}Sr/^{90}Y$ source as measured by a 10.2 mm BC-400 plastic scintillator.

energy and detector dimensions,[18] i.e., the larger the scintillator, the greater the likelihood of multiple scattering. Occurrence of multiple scattering events is indicated when an amount of energy is deposited in the detector which is greater than the maximum recoil electron energy. The 10.2 mm BC-400 plastic scintillator is a relatively small detector, and therefore the probability of multiple scattering is low. The position of the maximum recoil electron energy with respect to the broadened Compton peak height demonstrates a slight energy dependence[19] and this position lies nearer to half of the peak height for small detectors than large detectors.[18]

Gamma ray resolution also exhibits energy dependence and is estimated through analysis of the Compton edge. Resolution is defined as twice the half width at half of the Compton peak value divided by the peak position. Figure 3.3. depicts the variation of measured resolution with maximum recoil electron energy for a 10.2 mm BC-400 plastic scintillator detector.

An example of the spectrometer's response to 0.662 MeV gamma rays is presented in Fig. 3.4.

2. The Spectrometer Assembly

The beta spectrometer utilized in acquiring beta particle energy distributions from a beta beam flattening filter system consisted of a detector assembly and associated electronics.

a. Detector assembly. The detector assembly comprised the following major apparatus: plastic scintillator detector, optical coupling grease, a photomultiplier tube, voltage divider string, and a magnetic shield. The 10.2 mm thick BC-400 detector has characteristics

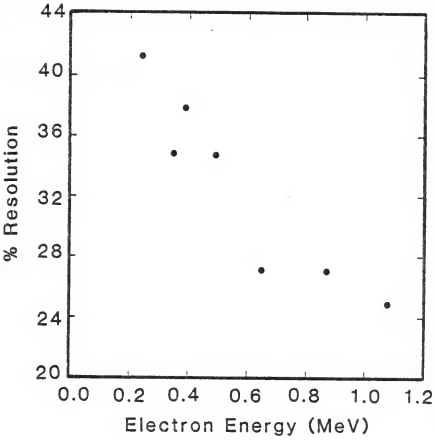

FIG. 3.3. Resolution of a 10.2 mm BC-400 plastic scintillator based spectrometer as a function of maximum Compton recoil electron energy. Values were determined through the analysis of Compton recoil electron pulse height distributions.

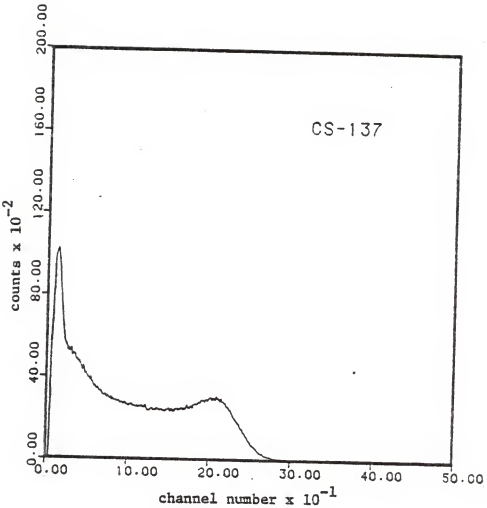

FIG. 3.4. Pulse height distribution measured with a 10.2 mm BC-400 plastic scintillator based spectrometer for 0.662 MeV gamma rays from ^{137}Cs.

which are provided in Table 3.1. The detector was optically coupled to the 50.8 mm diameter pyrex window of a 12 stage RCA Model 8575 photomultiplier tube with BC-630 optical coupling grease. The sides of the detector were lined with 1 mil aluminum foil reflector followed by 7 mil black vinyl plastic tape to provide a light-tight seal. A 9 μm aluminum foil entrance window was mounted to the upper face of the detector and was secured by 7 mil black vinyl plastic tape, leaving a sensitive detector window area of approximately 7 cm^2. An RCA Model AJ2207A voltage divider string regulated interdynode potentials in the photomultiplier tube. And, the entire assembly was enclosed by a Perfection Mica Company Model 25P50N precision magnetic shield to protect the photomultiplier from stray magnetic fields as well as the earth's magnetic field. A 9 mm thick high density polyethylene collimator was placed on the top of the assembly to reduce bremsstrahlung photon generation in the upper edge of this magnetic shield. A diagram of the detector assembly is presented in Fig. 3.5.

b. Associated electronics. The associated electronics consisted of a high voltage power supply, a preamplifier, a preamplifier power supply, linear amplifier, and a multichannel analyzer.

A voltage of -1500V was supplied to the voltage divider string by a Canberra Model 30002 high voltage power supply. Impedance matching between the detector assembly and linear amplifier was provided by a Canberra Model 2005E preamplifier powered by a Tennelec Tennebin Model 3. The detector signal was amplified by a Canberra Model 2013 linear amplifier and pulse height data were collected by a Canberra Series 80 multichannel analyzer, using 1024 data channels for each spectrum. Data

Table 3.1. Characteristics of a BC-400 plastic scintillator used in the evaluation of the beam flattening filter.

Description	Value
Diameter	50.8 mm
Thickness	10.2 mm
Base	Polyvinyltoluene
Density	1.032 g cm^{-3}
Melting point	75°C
Refractive index	1.581
Decay constant (main component)	2.4 nsec
Light output	65% Anthracene
Wavelength of maximum transmission	42.3 nm
Coefficient of lilnear expansion	$\sim$7.8 x 10^{-5} below 67°C
H/C atomic ratio	1.104

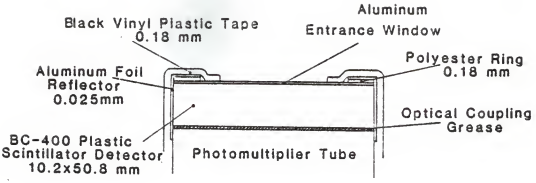

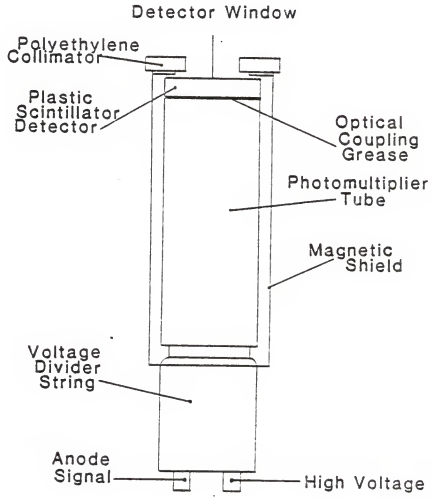

FIG. 3.5. Diagram of the detector assembly used in the beta spectrometer.

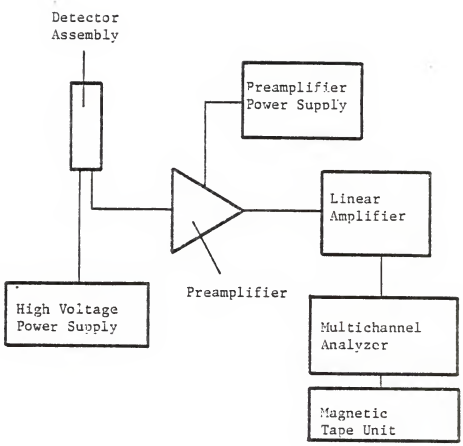

FIG. 3.6. Schematic diagram of the plastic scintillator based beta spectrometer.

were stored on magnetic tape for computer analysis. A simple block diagram of the beta spectrometer is provided in Fig. 3.6.

3. Energy Calibration

As experienced in the past, the energy calibration of the plastic scintillator based spectrometer was difficult and the method chosen involved two separate calibrations with gamma ray and beta particle emitters. A rough energy calibration was first estimated on the basis of analyses of Compton pulse height distributions. The preliminary calibration was then used in the analyses of measured beta spectra, which provided the beta endpoint position estimates used to determine the final energy calibration. Care was taken to conduct all calibration measurements at count rates below 1,000 counts per second, so that dead time losses were negligible and to avoid photomultiplier tube fatigue resulting in an apparent gain shift in the system.

a. Calibration with Compton distributions. Compton distributions were collected with the spectrometer for the following gamma photon sources: ^{137}Cs, ^{113}Sn, ^{22}Na, ^{54}Mn, and ^{207}Bi. These spectra were measured with a 222 mg/cm^2 high density polyethylene absorber present between source and detector to eliminate the contribution of any beta particles or internal conversion electrons below approximately 0.6 MeV to the Compton distributions. In order to estimate the position of the maximum recoil electron energy, the broadened Compton peak position had to first be identified. The task is relatively easy for well defined Compton peaks from low energy gamma rays, but is difficult in the case of poorly defined peaks from higher energy gamma rays. Therefore a standard

method of analysis was adopted for locating the Compton peak position, and determining peak height and resolution. Basing the analysis on the assumption that the Compton distribution could be approximated by a Gaussian model near the Compton peak region, a Gaussian distribution was fit to data points on the Compton edge. The technique[16] involved linearizing the data and performing a linear least squares analysis to calculate a slope and intercept which were used to estimate the peak position and standard deviation. The peak height was estimated from a weighted mean of the data. Figure 3.7 provides an example of linearized data from a ^{22}Na Compton distribution measured with a 10.2 mm BC-400 plastic scintillator based spectrometer. The solid line was determined through a weighted linear least squares fit to the data. A detailed description of the analysis is provided in Appendix C.

The model appeared to effectively approximate distributions from gamma photons with energies between 0.392 and 1.275 MeV. Figures 3.8 and 3.9 illustrate the success of the analysis in approximating Compton spectra near the edge regions of ^{22}Na and ^{113}Sn pulse height distributions measured with a 10.2 mm BC-400 plastic scintillator. A five point data smoothing routine[21] was incorporated in the analysis to smooth poorly defined Compton edges from ^{54}Mn and ^{22}Na, but smoothing altered peak position estimates by less than 1%. Table 3.2 presents the results of Compton distribution analyses.

Choosing 70% of the Compton peak heights as the channel positions representing maximum recoil electron energies on the basis of work performed by other investigators,[19,22] a linear least square fit to these data provided a preliminary energy calibration for the spectrometer.

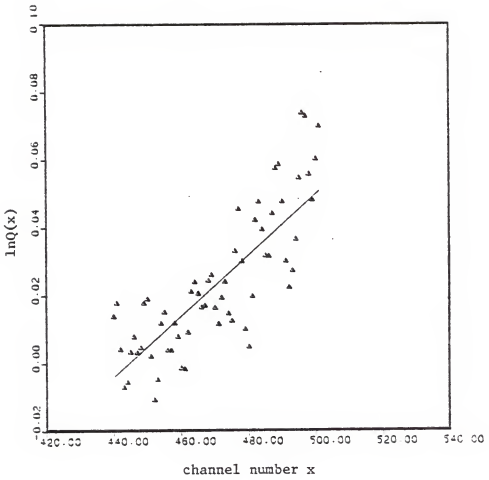

FIG. 3.7. Linearized data from a portion of a measured ^{22}Na Compton recoil electron pulse height distribution with a least squares fit line used to estimate the Compton peak centroid position and resolution.

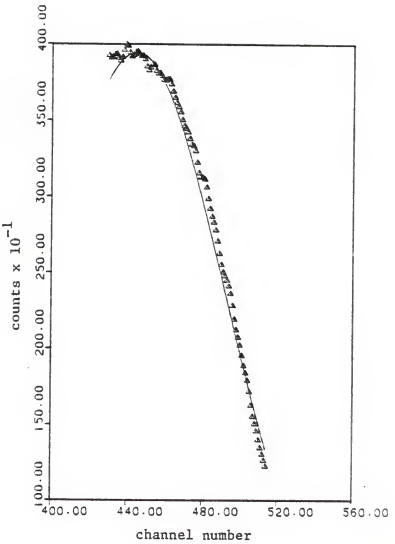

FIG. 3.8. A portion of a measured ^{22}Na Compton recoil electron pulse height distribution with a line representing the least squares fit of a Gaussian model to the data along the Compton edge. The maximum recoil electron energy is 1.062 MeV.

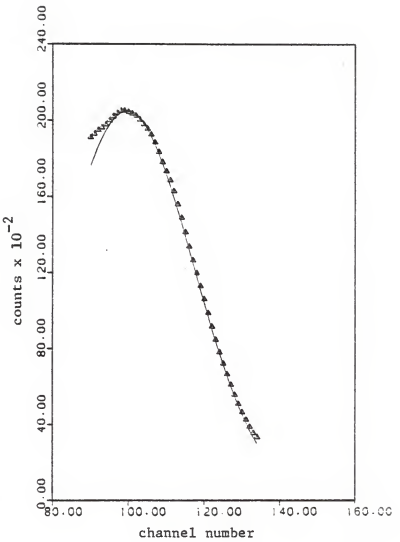

FIG. 3.9. A portion of a measured ^{113}Sn Compton recoil electron pulse height distribution with a line representing the least squares fit of a Gaussian model to the data along the Compton edge. The maximum recoil electron energy is 0.237 MeV.

Table 3.2. Results of Compton edge analyses for the calibration of a 10.2 mm BC-400 plastic scintillator based spectrometer.

Isotope	E_γ (MeV)	Yield (%)	$E_{e^-_{max}}$ (MeV)	x_o (Ch. no.)	σ (Ch.)	resolution (%)
$^{113}_{50}Sn$	0.3917	64.0	0.2371	99.76	17.46	41.21
$^{137}_{55}Cs$	0.6616	85.0	0.4773	201.19	29.60	34.65
$^{54}_{25}Mn$	0.8348	100.0	0.6392	280.97	32.26	27.04
$^{207}_{83}Bi$	0.5697	97.7	0.3933	164.32	26.38	37.81
	1.0636	74.0	0.8576	355.94	40.90	27.06
$^{22}_{11}Na$	0.5110	180.8	0.3407	148.78	22.01	34.84
	1.2746	99.9	1.0618	444.69	47.13	24.96

Other percentages of the Compton peak height were tested as positions of maximum recoil electron energies and regression analyses indicated that linear models with no intercept best characterized the relationship between electron energy and channel number for 100% - 70% experimental results. Second order channel number dependence tended to increase with decreasing percentage and results using fractional Compton peak height positions below 70% exhibited small but definite second order dependence, with all parameter estimates significant above the 95% confidence level.

b. Calibration with beta endpoints. The next step in energy calibration of the spectrometer involved calculation of Kurie plot values over regions of measured beta spectra. Pulse height distributions were collected for the following beta particle emitters: ^{14}C, ^{45}Ca, ^{185}W, $^{90}Sr/^{90}Y$, ^{36}Cl, ^{204}Tl, and ^{32}P with known endpoints from 0.155 to 2.288 MeV. Fermi function values were estimated with the relativistic model presented in Section 2 and Kurie plot values were calculated by Eq. 2.21. The preliminary energy calibration was used to determine total relativistic energies corresponding to channel numbers.

Some Kurie plots of measured data exhibited deviations from linearity in low energy and high energy regions due to distortion of the spectrum shape from source backscattering as well as other distortive effects discussed in Section 3.B. Generally, the region just below the high energy end of the Kurie plots was linear and the extrapolation from a linear least squares fit line in this region to the total relativistic energy axis provided an estimate of the endpoint of the beta pulse height distribution. Figures 3.10 - 3.13 present measured beta particle energy distributions and their corresponding Kurie plots along with absorption

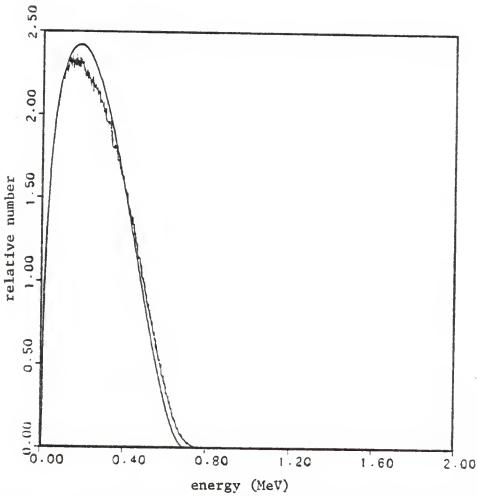

FIG. 3.10. Measured and theoretical normalized ^{36}Cl beta particle energy distributions. Measured data were obtained with a 10.2 mm BC-400 plastic scintillator and the theoretical distribution was estimated by the relativistic model with a correction for window absorption.

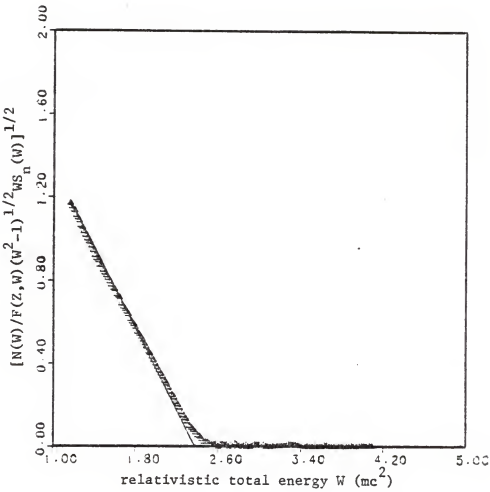

FIG. 3.11. Measured and theoretical Kurie plots of a ^{36}Cl beta particle energy distribution. A 10.2 mm BC-400 plastic scintillator was employed to collect the data and the theoretical plot was derived from the relativistic model with a correction for window absorption.

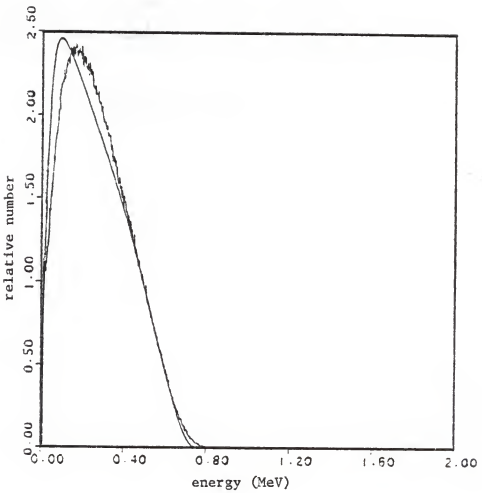

FIG. 3.12. Measured and theoretical normalized ^{204}Tl beta particle energy distributions. Measured data were obtained with a 10.2 mm BC-400 plastic scintillator and the theoretical distribution was estimated by the relativistic model with a correction for window absorption.

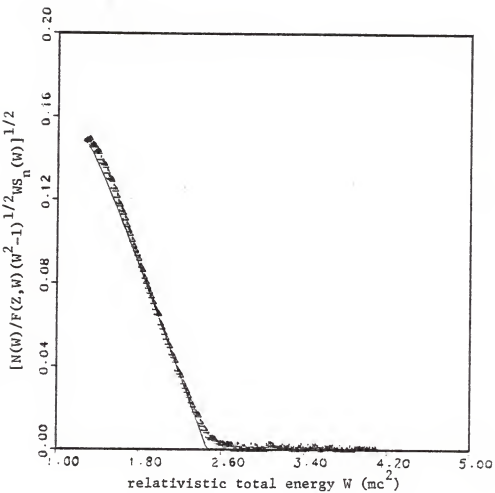

FIG. 3.13. Measured and theoretical Kurie plots of ^{204}Tl beta particle energy distributions. Measured data were obtained with a 10.2 mm BC-400 plastic scintillator and the theoretical plot was derived from the relativistic model with a correction for window absorption.

corrected theoretical models for ^{36}Cl and ^{204}Tl. A least square fit of estimated channel endpoints and absorption corrected known endpoint energies provided the final energy calibration for the 10.2 mm BC-400 plastic scintillator based spectrometer.

C. The $^{90}Sr/^{90}Y$ Beta Source

The beta source used in the evaluation of the beam flattening filter was a 30 μCi $^{90}Sr/^{90}Y$ capsule manufactured by Isotope Products Laboratories. The active deposit was $SrTiO_3$, with a 0.254 mm silver backing encapsulated in 304L stainless steel. The source was provided with a 0.254 mm beryllium window of mass thickness approximately 46.9 mg cm^{-2}. To reduce particle scattering from the sides and back of the source and to reduce bremsstrahlung radiation, the entire capsule was mounted in a polyethylene cylinder. A diagram of the source is presented in Fig. 3.14.

Radiation emitted from the source included beta particles, gamma rays, and X-rays. Beta particles emitted through the first forbidden unique decay of $^{90}_{38}Sr$ ($t_{\frac{1}{2}}$ = 28.8y) to $^{90}_{39}Y$ possess an endpoint energy of 0.546 MeV, but through attenuation in the beryllium window, the residual beta particle energy was calculated to be 0.443 MeV. As a result of this decay, ^{90}Y was present at an equilibrium concentration with the ^{90}Sr, and with a half life of 64.06 h, beta particles were emitted through the first forbidden unique decay of ^{90}Y with an endpoint energy of 2.288 MeV (2.200 MeV when corrected for window losses). All beta particles emitted from the source material with energies below approximately 0.215 MeV were attenuated in the beryllium window. Two gamma rays of energies 1.761 MeV and 2.186 MeV were present, but their yields of 3.4 x 10^{-3}% and 1.4 x

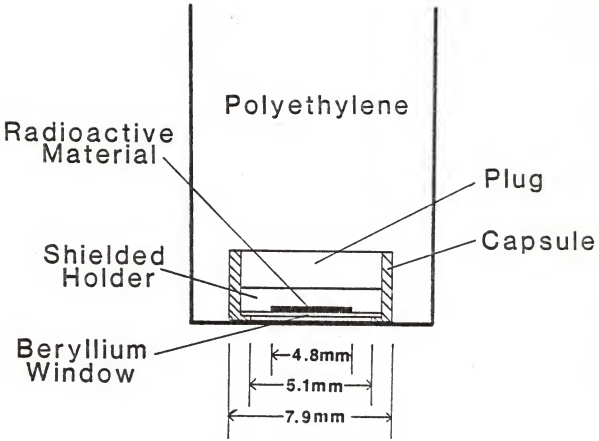

FIG. 3.14. Diagram of the $^{90}Sr/^{90}Y$ beta source.

10^{-6}% respectively were too low to have an impact on measured spectra. Bremsstrahlung photons were generated as beta particles were attenuated in the source material and encapsulation. And, characteristic X-rays were produced as beta particles excited Fe and Ag atoms in the encapsulation. The $K_{\alpha 1}$ X-rays of Fe and Ag have energies of 6.4 keV and 22.2 keV respectively.

IV. DATA ACQUISITION AND ANALYSIS

A. Measuring beam flattener attenuated $^{90}Sr/^{90}Y$ beta spectra.

Pulse height distributions were collected with the beta spectrometer to evaluate a $^{90}Sr/^{90}Y$ beta beam flattening filter. With the spectrometer on the central axis of the system (zero displacement), data were collected for 6000 seconds. Figure 4.1 illustrates the measured energy distribution of radiation emitted from the $^{90}Sr/^{90}Y$ source at zero displacement in the beam flattening system. As a consequence of characteristic X-ray emissions from the source which interacted in the scintillator by photoelectric absorption, a peak was located in the low energy region of the spectra corresponding to the $K_{\alpha 1}$ X-ray from Ag in the source encapsulation. To eliminate the low energy photon contribution to measured distributions, a low Z polymethylmethacrylate absorber with a mass thickness of approximately 861 mg cm^{-2} was positioned over the detector window. The absorber was of sufficient mass thickness to attenuate nearly all beta particles scattered toward the detector. Next, the multichannel analyzer was operated in the subtract mode for 6000 seconds to obtain a pulse height distribution with negligible X-ray, background photon, and noise components. This procedure was repeated with the spectrometer assembly positioned off axis in 2 cm increments across the calibration plane to collect several pulse height distributions for computer analysis. To evaluate the effect of the presence of a beam flattening filter on spectrum shape and dose uniformity, another set of pulse height distributions was collected by the same procedure in the absence of the filter. Finally, a data set was collected with the beam flattening filter located at 20 cm from the

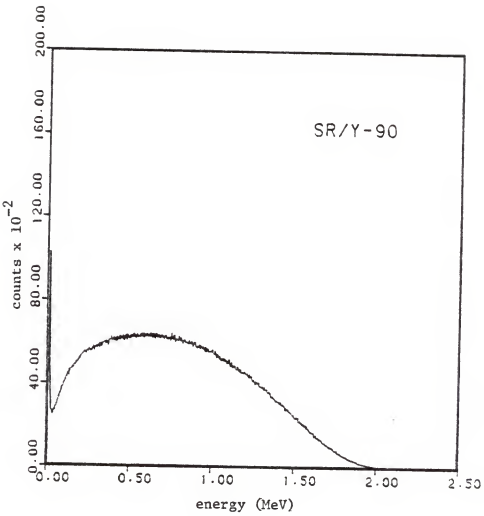

FIG. 4.1. Energy distribution of radiation arriving at the center of the calibration plane in the $^{90}Sr/^{90}Y$ beta beam flattening filter system as measured by a 10.2 mm BC-400 plastic scintillator based spectrometer with a 2.43 mg cm^{-2} aluminum window.

source to examine the effect of filter position on spectrum shape and dose uniformity.

B. Analysis of the attenuated $^{90}Sr/^{90}Y$ spectra

Through computer analysis of pulse height distributions collected with the beta spectrometer, the variation in absorbed dose at the calibration distance was estimated for the $^{90}Sr/^{90}Y$ beta beam flattening system. Absorbed dose in a material may be described[7] by considering the amount of energy $\Delta\varepsilon$ imparted by ionizing radiation to a small incremental volume of material ΔV at some position with mass Δm:

$$D = \lim_{\Delta V \to 0} \frac{\Delta\varepsilon}{\Delta m}, \qquad (4.1)$$

in which statistical variation is ignored in the limiting process. Thus, the absorbed dose to a quantity of matter from beta particles is affected by the number of particles interacting in the volume and average beta particle energy. As a result of the spectrometer's efficiency for detecting beta particles and because pulse height distributions provided an indication of the energy spectrum of the particles attenuated in the beam flattening filter system, the product of the integral number of counts and estimated average energy of a measured beta particle energy spectrum was assumed to be related to the absorbed dose at the calibration distance. With the presence of the aluminum detector window, the product was actually related to the absorbed dose in a material at a depth of 2.43 mg cm^{-2}. The true absorbed dose at a depth of 2.43 mg cm^{-2} in a material at the calibration area is dependent upon the flux density energy spectrum of charged particles, the type of material, and the rate

of energy transfer per unit path length of the beta particles to the material, assuming that nuclear reactions are negligible and electronic equilibrium is maintained.

The variation in absorbed dose was estimated by comparing these products for distributions collected across the calibration plane. The integral number of counts in each spectrum was determined by a simple summation of the number of counts recorded in each channel:

$$C = \sum_{i=1}^{n} N(E_i)\ \Delta E_i, \tag{4.2}$$

where $N(E_i)$ represents the number of counts recorded in channel i of width ΔE_i with average energy E_i, and n equals the total number of channels. The uncertainty associated with C was equal to $C^{\frac{1}{2}}$ since the counting process was governed by Poisson statistics. No correction of the integral counts for source decay was performed. This correction was assumed to be negligible due to the long half life of the source and because data sets were collected over a short period of time. Average energies of the measured spectra were estimated by the following expression:

$$\bar{E} = \frac{\sum_{i=1}^{n} E_i N(E_i)\Delta E_i}{\sum_{i=1}^{n} N(E_i)\ \Delta E_i}. \tag{4.3}$$

The simple calculation was assumed to provide adequate accuracy on the basis of past work.[23] The deviation of the absorbed dose at points across the calibration plane from the absorbed dose on the central axis of the system was estimated by comparing the product of $C\bar{E}$ from several

spectra. Data collected at distance x from the axis on the calibration plane were compared to data from the central axis (x=0) as follows:

$$\frac{D_x - D_o}{D_o} \cong \frac{C_x\bar{E}_x - C_o\bar{E}_o}{C_o\bar{E}_o} = Var_x. \qquad (4.4)$$

Thus 100 Var_x represents an estimate of percent deviation of the absorbed dose at position x from the absorbed dose on the central axis of the system.

Statistical error in the absorbed dose variation indicator Var_x was primarily dependent upon errors associated with the average energy estimate and hence upon the energy calibration of the spectrometer. As the quantity was only used as an estimate of absorbed dose variation, the statistical error was not evaluated for each indicator. Other errors in the estimates include those due to pulse height distortion effects discussed in Section 3.B.

V. RESULTS AND CONCLUSIONS

A. Results of the spectral analyses

Data collected from the three experimental configurations of the $^{90}Sr/^{90}Y$ beta beam flattening system were analyzed to estimate the success of the system in providing a uniform absorbed dose at the calibration plane.

Figure 5.1 illustrates the measured energy spectrum (at zero displacement) of beta particles attenuated in the system with the filter at 10 cm from the source. The corresponding Kurie plot is depicted in Fig. 5.2. Both figures include a theoretical distribution based on the relativistic model with a correction simulating particle attenuation in air, the filter, and in the source and detector windows. The estimated average energy of the measured distribution was 0.8137 MeV, only 5.2 keV greater than the average energy of the calculated spectrum. The major difference in shape is attributed to resolution broadening clearly evident in the high energy region.

The variation of measured spectrum areas with increasing detector displacement was considerably different for each of three experimental beam flattener system configurations, and results are presented in Fig. 5.3. For the case in which the beam flattening filter was removed, the spectral areas decreased with increasing detector displacement as a consequence of the reduction of the solid angle subtended by the detector surface. The solid angle decreased by a factor of cosine α, in which α was the angle between the normal to the detector surface and a line between the source and center of the detector window. With the filter placed at 10 cm from the $^{90}Sr/^{90}Y$ source, the spectrum area varied less

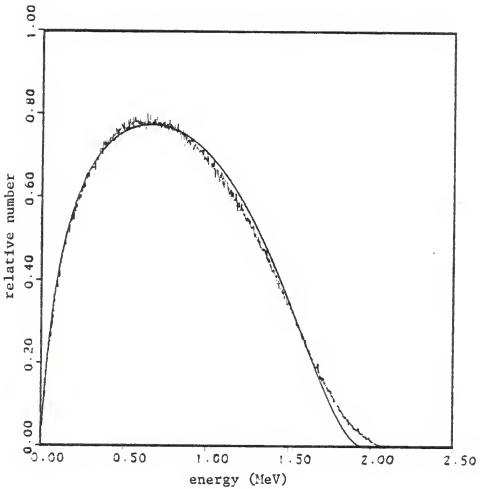

FIG. 5.1. Measured and calculated energy distribution of $^{90}Sr/^{90}Y$ beta particles attenuated in a beam flattening filter system with the filter at 10 cm from the source. Measurements were performed with a 10.2 mm BC-400 plastic scintillator at the central axis of the calibration plane. The theoretical distribution is based upon the relativistic model with an absorption correction.

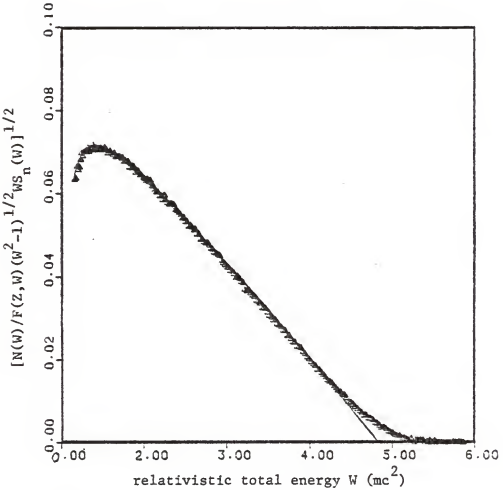

FIG. 5.2. Calculated and measured Kurie plots for the energy distribution of $^{90}Sr/^{90}Y$ beta particles attenuated in a beam flattening filter.

than ± 3.1% for detector displacements of 10 cm or less, while the area increased for increasing detector displacement by 21.7% over the value at zero displacement when the filter was positioned 20 cm from the source.

Estimated changes in average energies and percent deviation of average energies are presented in Figs. 5.4 and 5.5 respectively for all three trials. In the absence of the beam flattening filter, average beta energy increased from 800.6 to 819.2 keV over the 10 cm radius of the calibration area. The presence of the filter increased average energies and for a filter position at 10 cm from the source, the estimated average energy increased from 813.7 to 834.9 keV over the calibration area. With the filter at 20 cm from the source, the average energy increased from 816.2 keV to 830.8 keV. Generally, as demonstrated by Fig. 5.5, the average energies increased by approximately 2% over the calibration area with 10 cm radius for all three trials.

The absorbed dose variation indicator Var_x is presented as a function of increasing detector displacement in Fig. 5.6 for all experimental trials. The dose variation indicator decreased as detector displacement increased, with a maximum deviation of -11.3% for the case in which no filter was present. When the beam flattening filter was positioned at 20 cm from the source, Var_x increased with increasing displacement, and the maximum deviation was +23.9%. But for the case with the filter at 10 cm, the indicator remained virtually unchanged with variation between +0.04% and -1.55%, for detector displacements up to 10 cm.

B. Conclusions

On the basis of the comparison between theoretical and measured spectra, the relativistic model with an absorption correction based on an

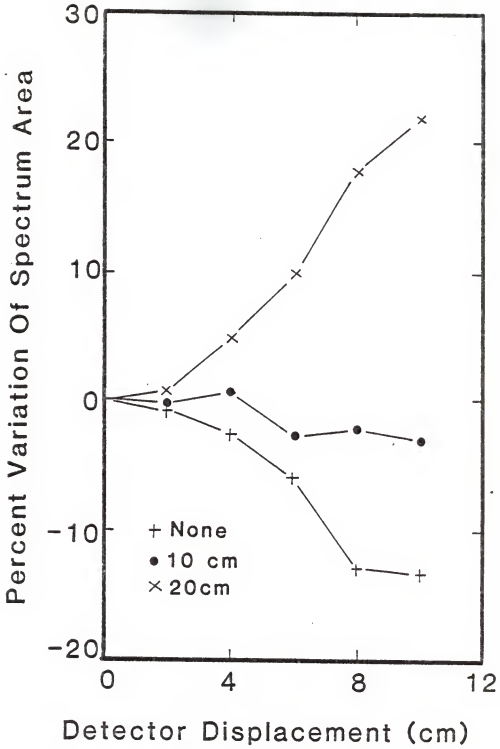

FIG. 5.3. Percent variation in the area of measured $^{90}Sr/^{90}Y$ beta particle energy distributions for increasing detector displacement along the calibration plane with no beam flattening filter present, and with the filter at 10 cm and 20 cm from the source.

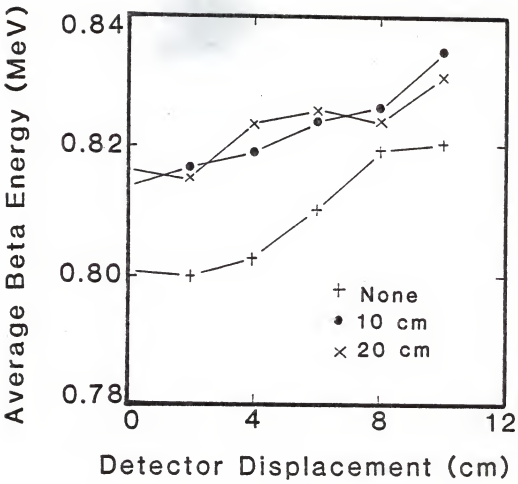

FIG. 5.4. Average energy of measured $^{90}Sr/^{90}Y$ beta particle energy distributions for increasing detector displacement along the calibration plane with no beam flattening filter present, and with the filter at 10 cm and 20 cm from the source.

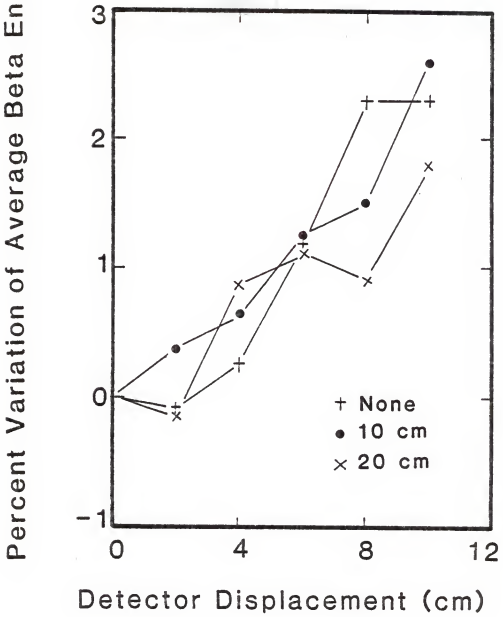

FIG. 5.5. Percent variation in the average energy of measured $^{90}Sr/^{90}Y$ beta particle energy distributions for increasing detector displacement along the calibration plane with no beam flattening filter present, and with the filter at 10 cm and 20 cm from the source.

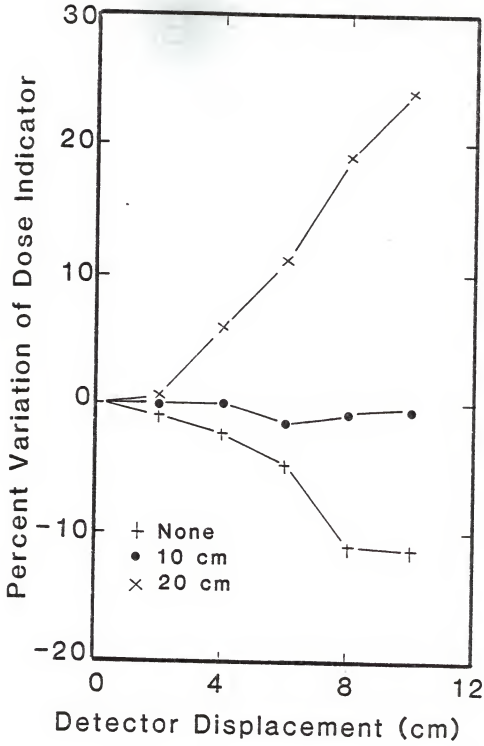

FIG. 5.6. Percent variation in the absorbed dose indicator Var estimated through the analysis of measured $^{90}Sr/^{90}Y$ beta particle energy distributions for increasing displacement from the center of the calibration area in a beam flattening filter system. Results are presented for cases in which no beam flattening filter was present, and with the filter at 10 cm and 20 cm from the source.

electron range-energy relationship developed by Katz and Penfold (for aluminum) adequately estimates the energy distribution of $^{90}Sr/^{90}Y$ beta particles attenuated in the beam flattening filter system with the filter at 10 cm from the source. But, the approximation is limited in that the model does not include a correction for spectrum distortions such as those created by resolution broadening in the spectrometer, and it does not account for spectral shape changes related to the position of the filter between the source and calibration area.

The $^{90}Sr/^{90}Y$ beta beam flattening filter appears to substantially reduce variations in absorbed dose over a calibration area 20 cm in diameter as suggested by other investigations.[3,4,5] For the particular experimental beam flattening filter configuration evaluated in this research, the absorbed dose at a depth of 2.43 mg cm^{-2} was estimated to vary less than ±1.6% over the calibration area. The presence of the filter definitely increased the average energy of beta particles arriving at the calibration area, but the filter's presence and position had little effect on the manner in which the average energy varied over the calibration region, as demonstrated by Fig. 5.5. This behavior in the average energy resulted in the similarity between Figs. 5.3 and 5.6, suggesting that the absorbed dose variation is most strongly influenced by the variation in the number of beta particles arriving at the calibration area. Thus, the estimation of absorbed dose variation on the basis of integral count or count rate behavior over the calibration area is approximately valid when evaluating the $^{90}Sr/^{90}Y$ beta beam flattening filter.

The absorbed dose uniformity at the calibration plane is sensitive to filter position and variation is minimized only for a specific geometric configuration. For the particular filter investigated, the

results suggest that the absorbed dose at a point on the calibration area tends to increase with increasing distance from the central axis as the distance between source and filter is increased.

VI. SUGGESTIONS FOR FURTHER STUDY

The ultimate application of the beta beam flattening filter evaluated in this research will involve dosimetry studies with beta sensitive thermoluminescent dosimeters and an experiment should be performed to determine the absorbed dose uniformity in dosimeters at the calibration plane. The experiment should entail the dosing of several calibrated dosimeters (so that their relative response is known) positioned at points across the calibration plane. The absorbed dose uniformity may be determined by comparing the readouts of the dosimeters. The beam flattening filter should also be mounted in a framework consisting of low Z materials for precise control of the system geometry and it is suggested that several different source-filter-calibration plane geometric arrangements be tested.

Calculations and experiments might also be performed to develop new filter designs. Filters designed for use with beta sources other than $^{90}Sr/^{90}Y$ should be investigated and efforts might be made to enlarge the calibration area over which the absorbed dose is uniform, without sacrificing the practical geometry of the system.

VII. ACKNOWLEDGMENTS

I would like to express my sincere appreciation to Dr. G. G. Simons for his advice and guidance during the course of this research and during the preparation of this thesis. I am also grateful to R. B. Stuewe and J. Higginbotham for their assistance and suggestions.

VIII. REFERENCES

1. P. Plato, Int. J. of Appl. Rad. and Isot., 30, 109 (1979).

2. American National Standards Institute, Criteria for Testing Personnel Dosimetry Performance, ANSI N13.11, (1982).

3. International Organization for Standardization, Reference Beta Radiations for Calibrating Dosemeters and Doseratemeters and for Determining their Response as a Function of Beta Radiation Energy, ISO/DIS 6980 (1983).

4. Buchler GmbH & Co., Manual for the Beta Secondary Standard, September 1979.

5. B. Owen, Phys. Med. Biol., 17, 177-179 (1972).

6. T. Dakubu, Int. J. of Appl. Rad. and Isot., 29, 717-720 (1978).

7. A.B. Chilton, J.K. Shultis, and R.E. Faw, Principles of Radiation Shielding (Prentice-Hall, Englewood Cliffs, New Jersey, 1983) pp. 67-74.

8. L. Katz and A.S. Penfold, Rev. of Mod. Phys., 24, 28 (1952).

9. P.C. Rogers and G.E. Gordon, Nucl. Instr. and Meth., 37, 262 (1965).

10. R.E. Lapp and H.C. Andrews, Nuclear Radiation Physics, 4th ed. (Prentice-Hall, Englewood Cliffs, New Jersey, 1972) p. 218.

11. A.C.G. Mitchell, in Beta- and Gamma-Ray Spectroscopy, edited by K. Siegbahn (North-Holland, Amsterdam, 1955) pp. 240-245.

12. T.R. England and M.G. Stamatelatos, LA-6445-MS, (1976).

13. J. Mantel, Int. J. of Appl. Rad. and Isot., 23, 408-413 (1972).

14. W.G. Cross (private communication).

15. E.J. Konopinski, The Theory of Beta Radioactivity, (Oxford, London, 1966) pp. 2-15.

16. R.B. Stuewe, "Evaluation of Plastic Scintillator and High-Purity Germanium Detectors for use in Beta Spectroscopy," Master's Thesis, Kansas State University (1982).

17. D.M. Rehfield and R.B. Moore, Nucl. Instr. and Meth., 157, 365-387 (1978).

18. G. Dietze and H. Klein, Nucl. Instr. and Meth., 193, 551 (1982).

19. J.G. Cramer Jr., B.J. Farmer, and C.M. Class, Nucl. Instr. and Meth., 16, 294 (1962).

20. G.F. Knoll, Radiation Detection and Measurement, (John Wiley & Sons, New York, 1979) pp. 735-739.

21. P.R. Bevington, Data Reduction and Error Analysis for the Physical Sciences, (McGraw-Hill, New York, 1969) pp. 255-263.

22. E. Nardi, Nucl. Instr. and Meth., 95, 229-232 (1971).

23. G.G. Simons, T.M. DeBey, R.B. Stuewe, and K.D. Stansbury, "Application of Beta Spectroscopy to Beta Dosimetry Research," presented at the International Beta Dosimetry Symposium, Washington D.C., 1983 (unpublished).

APPENDIX A: EFFECT OF ABSORPTION CORRECTION ON CALCULATED KURIE PLOTS

Kurie plots were calculated for theoretical beta particle energy distributions in an effort to determine the effect of absorption losses on Kurie plot shapes. A relativistic model was used to estimate the spectra and the absorption correction was based on an electron range-energy relationship developed by Katz and Penfold.[a] Figures A.1 - A.3 represent Kurie plots of ^{36}Cl, ^{185}W and combined $^{90}Sr/^{90}Y$ spectra for various absorber mass thicknesses. The correction of theoretical Kurie plots for absorption losses introduced a non-linearity into the plots and in general, the degree of non-linearity increased with increasing absorber thickness. The low energy portions of the plots exhibited strong non-linearity, while high energy regions were only slightly influenced. The Kurie plots intercept the W-axis at positions representing the maximum relativistic total energy with correction for the presence of the indicated absorber thickness.

Reference:

[a] L. Katz and A. S. Penfold, Rev. of Mod. Phys., 24, 28 (1952).

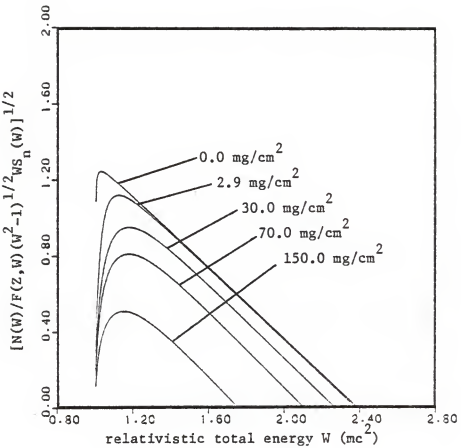

FIG. A.1. Calculated Kurie plot for the ^{36}Cl beta particle energy distribution as a function of increasing absorber thickness. Plots were determined by the relativistic model with an absorption correction.

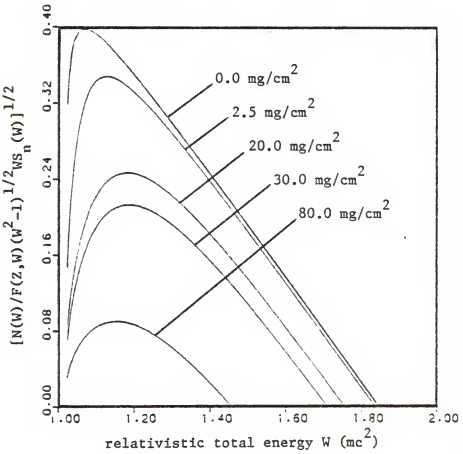

FIG. A.2. Calculated Kurie plot for the ^{185}W beta particle energy distribution as a function of increasing absorber thickness. Plots were determined by the relativistic model with an absorption correction.

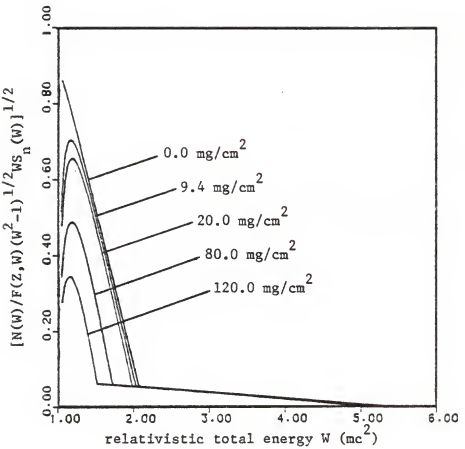

FIG. A.3. Calculated Kurie plot for the combined $^{90}Sr/^{90}Y$ beta particle energy distribution as a function of increasing absorber thickness. Plots were determined by the relativistic model with an absorption correction.

APPENDIX B: RESOLUTION BROADENING

When the pulse height distribution of a beta or gamma emitter is measured with a plastic scintillator based spectrometer, the spectrum shape is distorted by resolution broadening. Resolution broadening occurs primarily as a result of the statistical nature of the collection of photons by the photomultiplier tube and is thus dependent upon the particular spectrometer used to record data and upon the energies of the incident radiation. Factors affecting the energy resolution of the spectrometer include: scintillator fluorescent efficiency, light collection efficiency, photocathode efficiency and uniformity, photoelectron collection efficiency, the secondary emission coefficient, and photomultiplier and amplifier noise. As a result of these effects, the pulse height distribution for monoenergetic electrons interacting in the scintillator is not a delta function.

To investigate this effect, resolution broadening was simulated mathematically by distorting a theoretical beta energy response spectrum (or a theoretical Compton spectrum in the case of gamma-ray interactions in a plastic scintillator) with an energy dependent broadening function. Through the distortion of the theoretical spectra, changes in spectrum shape, in beta energy endpoint, and in average beta energy were estimated.

A theoretical energy response function N(E') and the broadened spectrum g(E) are related as follows:

$$g(E) = \int_0^{E_{max}} N(E')F(E,E')dE', \qquad (B.1)$$

where F(E,E') is the broadening function. To evaluate the broadened spectra, the integral in Eq. (B.1) can be closely approximated by the summation

$$g(E_j) = \sum_{k=1}^{K} N(E_k)F(E_j,E_K)\Delta E_k, \tag{B.2}$$

provided that $N(E_k)$ and $F(E_j,E_K)$ vary slowly over ΔE_k.

The broadening function $F(E_j,E_k)$ approximates a detector's response to monoenergetic electrons of energy E_j and is a simple model in that energy losses within the source and detector cover are not accounted for. Since the measured pulse height distribution for monoenergetic electrons is very similar to a Gaussian distribution, the following Gaussian equation[b] was used to broaden the theoretical spectra:

$$F(E_j,E_k) = \frac{1}{\sqrt{\pi\sigma^2(E_j)}} \exp[-\tfrac{1}{2}(E_j-E_k)^2/2\sigma^2(E_j)]. \tag{B.3}$$

To apply Eq. (B.3), it was necessary to specify values for the standard deviation σ, which regulated the width of the broadening function centered at E_j. A model presented by Brietenberger,[c] who theoretically investigated the line broadening as a function of energy, was tested:

$$[\sigma(E_j)/E_j]^2 = A + B/E_j, \tag{B.4}$$

where the parameters A and B are related to factors affecting photoelectron production and collection in a scintillator based spectrometer. Equation (B.4), for small values of A, can be approximated by

$$\sigma(E) = B' \sqrt{E_j}. \qquad (B.5)$$

This equation was used to regulate line broadening in Eq. (B.3).

To test this concept, theoretical beta spectra were calculated for ^{36}Cl, ^{32}P, and ^{45}Ca using a relativistic model. These theoretical distributions were then broadened using Eqs. (B.2), (B.3), and (B.5) with B' = 0.089. As shown in Figs. B.1 - B.3, the broadened spectra extend significantly beyond the endpoints of the unbroadened spectra, but average beta energies remained essentially unchanged as a result of the broadening. In general these conclusions are valid. However, since the value for B' was an arbitrary choice, further study is necessary to determine the effect of resolution broadening for any specific organic scintillator.

Resolution broadening of Compton spectra was also investigated. The theoretical energy response function used in the analysis was the Compton differential scattering cross-section[d] derived by Klein and Nishina:

$$\frac{d(\sigma_e)}{dT} = \frac{\pi r_o^2}{\alpha m_o c^2} \{2 + \left(\frac{T}{E_o - T}\right)^2 [\frac{1}{\alpha^2} + \frac{E_o - T}{E_o} - \frac{2}{\alpha} \frac{(E_o - T)}{T}]\} \qquad (B.6)$$

where

$\alpha = E_o/m_o c^2$,

T = energy of the scattered electron in MeV,

E_o = energy of the incident photon in MeV,

$r_o = 2.818 \times 10^{-13}$cm, and

$m_o c^2 = 0.51098$ MeV,

= rest mass energy of the electron.

As an example result, the theoretical and calculated broadened Compton spectra for ^{137}Cs gamma-ray interactions are shown in Fig. B.4 (for B' = 0.089). Limited studies showed that the percentage of the broadened Compton peak height at which the maximum recoil electron energy intersected the distorted distribution tended to increase for increasing gamma ray energies. Moreover, the rate of increase was dependent upon the standard deviation σ chosen to regulate the broadening function.

References

[a] P.R. Bell, in Beta- and Gamma Ray Spectroscopy, edited by K. Siegbahn (North-Holland, Amsterdam, 1955) pp. 143-147.

[b] E. Nardi, Nucl. Instr. and Meth. 95, 229 (1971).

[c] E. Breitenberger, Progr. Nucl. Phys. 4, 56 (1956).

[d] R.D. Evans, in Radiation Dosimetry, 2nd ed., edited by F.H. Attix, W.C. Roesch, and E. Tochilin (Academic Press Inc., New York, 1968), Vol. 1, p. 106.

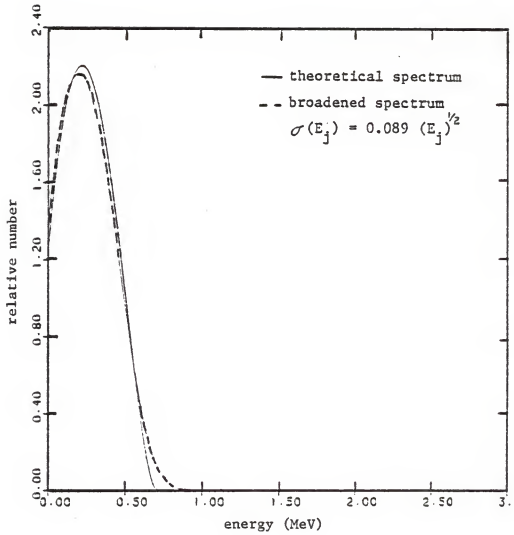

FIG. B.1. Theoretical and calculated broadened beta energy spectra for ^{36}Cl (E_o = 0.714 MeV and $\bar{E}$ = 0.270 MeV). The broadened spectrum average energy was 0.274 MeV.

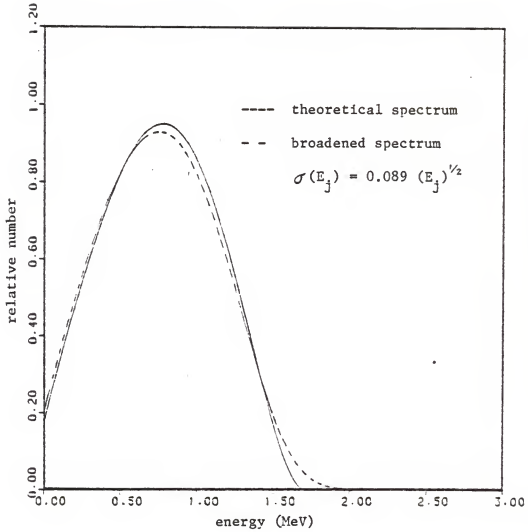

FIG. B.2. Theoretical and calculated broadened beta energy spectra for ^{32}P (E_o = 1.711 MeV and $\bar{E}$ = 0.765 MeV). The broadened spectrum average energy was 0.765 MeV.

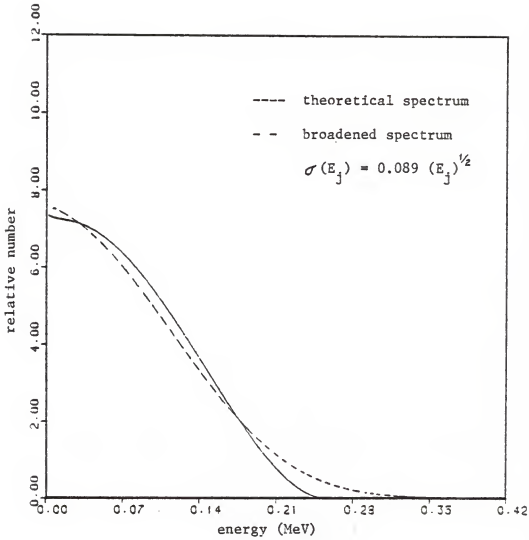

FIG. B.3. Theoretical and calculated broadened beta energy spectrum for ^{45}Ca (E_0 = 0.256 MeV, and $\bar{E}$ = 0.081 MeV). The broadened spectrum average energy was 0.086 MeV.

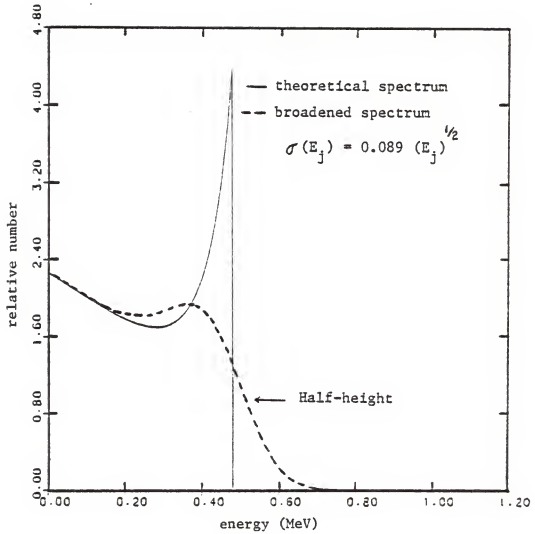

FIG. B.4. Theoretical and calculated broadened Compton recoil electron energy distribution from ^{137}Cs gamma rays.

APPENDIX C: COMPTON EDGE GAUSSIAN FITTING ROUTINE CALCULATIONS

Gamma rays with energies between 100 keV and 3 MeV primarily interact by Compton scattering in plastic scintillator detectors, and the resulting pulse height distribution of scattered electrons from a monoenergetic gamma photon source consists of a Compton edge with a slowly varying continuum down to zero energy. As a consequence of the finite energy resolution of the detector and associated electronics, the Compton edge is not a well defined point representing the maximum recoil electron energy. Assuming that this distorted edge may be represented analytically by a Gaussian equation, a method[a,b] was developed to least squares fit a Gaussian model to experimental Compton edge data. The method establishes a standard procedure for determining resolution and for designating percentage points along the edge as the position of the maximum recoil electron energy. The model takes the following form:

$$y(x) = y_o \exp[-(x-x_o)^2/2\sigma^2], \tag{C.1}$$

where $y(x)$ = Compton edge at position x,

y_o = maximum Compton peak height,

x_o = centroid of the Compton peak,

σ = standard deviation of the peak, and

x = channel number.

By linearizing the Gaussian model, σ and x_o can be determined for an experimental Compton pulse height distribution. The linearization is performed in the following manner:

$$\frac{y(x-1)}{y(x+1)} = \frac{\exp[-((x-1)-x_o)^2/2\sigma^2]}{\exp[-((x+1)-x_o)^2/2\sigma^2]}. \tag{C.2}$$

The expression on the right hand side of Eq. (C.2) may be reduced to obtain

$$\frac{y(x-1)}{y(x+1)} = \exp[2(x-x_o)/\sigma^2] = Q(x). \tag{C.3}$$

By taking the natural logarithm of both sides of Eq. (C.3), the following linear expression is obtained.

$$\ln\left\{\frac{y(x-1)}{y(x+1)}\right\} = \frac{2}{\sigma^2}x - \frac{2}{\sigma^2}x_o = \ln Q(x). \tag{C.4}$$

Thus, by least square fitting linearized data points with the simple linear model $\hat{Y}_i = \hat{\beta}_0 + \hat{\beta}_1 x_i$, σ and x_o are estimated accordingly:

$$\hat{\sigma} = (2/\hat{\beta}_1)^{\frac{1}{2}}, \text{ and} \tag{C.5}$$

$$\hat{x}_o = -\hat{\beta}_0/\hat{\beta}_1. \tag{C.6}$$

When performing the least squares fit, the data are weighted inversely with respect to their relative statistical variance, ΔY_i^2:

$$W_i = \frac{1}{\Delta Y_i^2} = \left[\frac{1}{y(x_i-1)} + \frac{1}{y(x_i+1)}\right]^{-1}. \tag{C.7}$$

Therefore, a data set is formed as such

$$Y_i = \ln\frac{y(x_i-1)}{y(x_i+1)}, \tag{C.8}$$

$$\Delta Y_i = \left[\frac{1}{y(x_i-1)} + \frac{1}{y(x_i+1)}\right]^{\frac{1}{2}}, \tag{C.9}$$

$$x_i = \text{channel number}, \tag{C.10}$$

$$\Delta x_i = 0, \text{ and} \tag{C.11}$$

$$W_i = \frac{1}{\Delta Y_i^2}, \tag{C.12}$$

where ΔY_i and Δx_i represent the standard errors for the linearized data points and channel numbers respectively.

A weighted least squares analysis[c] is executed with the following expressions for a data set of N pairs of observations,

$$A = \sum_{i=1}^{N} W_i, \tag{C.13}$$

$$B = \sum_{i=1}^{N} W_i x_i, \tag{C.14}$$

$$C = \sum_{i=1}^{N} W_i Y_i, \tag{C.15}$$

$$D = \sum_{i=1}^{N} W_i x_i^2, \text{ and} \tag{C.16}$$

$$E = \sum_{i=1}^{N} W_i Y_i x_i. \tag{C.17}$$

The linear model parameters $\hat{\beta}_0$ and $\hat{\beta}_1$ are estimated along with their associated errors $\Delta\hat{\beta}_0$ and $\Delta\hat{\beta}_1$ by the following relationships:

$$\hat{\beta}_0 = \frac{DC - BE}{AD - B^2}, \tag{C.18}$$

$$\Delta\hat{\beta}_0 = \frac{D}{AD - B^2}, \tag{C.19}$$

$$\hat{\beta}_1 = \frac{EA - BC}{AD - B^2}, \text{ and} \tag{C.20}$$

$$\Delta\hat{\beta}_1 = \frac{D}{AD - B^2}. \tag{C.21}$$

A maximum height y_o of the Gaussian model may be estimated from the measured data set by calculating the following weighted mean[a]:

$$\ln \hat{y}_o = \frac{\sum_{i=1}^{\hat{N}} W_i'[\ln y(x_i) + (x_i - \hat{x}_o)^2/2\hat{\sigma}^2]}{\sum_{i=1}^{N} W_i'}, \qquad (C.22)$$

where

$$W_i' = \left\{\frac{1}{y(x_i)} + \frac{(x_i - \hat{x}_o)^2}{\hat{\sigma}^4}\left\{(\Delta\hat{x}_o)^2 + \frac{(x_i - \hat{x}_o)^2}{\hat{\sigma}^2}(\Delta\hat{\sigma})^2\right\}\right\}^{-1}, \qquad (C.23)$$

$$(\Delta\hat{x}_o)^2 = \left(\frac{\Delta\hat{\beta}_o}{\hat{\beta}_1}\right)^2 + \left(\frac{\hat{\beta}_o}{\hat{\beta}_1}\right)^2 (\Delta\hat{\beta}_1)^2, \text{ and} \qquad (C.24)$$

$$(\Delta\hat{\sigma})^2 = \frac{(\Delta\hat{\beta}_1)^2}{2\hat{\beta}_1^3}. \qquad (C.25)$$

Data in the high energy region of the Compton edge are subject to distortions related to multiple scattering which cause the data to deviate from the Gaussian shape. Thus, only data from the peak region to a point near the middle of the Compton edge are included in the analysis to estimate the model parameters σ, x_o and y_o.

The energy resolution of the detector is defined for a Compton distribution as

$$\text{resolution} = \frac{2 \times \text{HWHM}}{\text{Compton peak position}}, \qquad (C.26)$$

where HWHM represents the half width of the Gaussian distributed edge data at half of the Compton peak height. The resolution may be estimated from the parameters obtained in the least squares analysis as follows:

$$\text{resolution} = \frac{2\sqrt{2\ln 2}\ \hat{\sigma}}{\hat{x}_o}. \tag{C.27}$$

The corresponding estimate of error in the calculated resolution is determined from Eq. (C.27):

$$(\Delta \text{ resolution})^2 = \frac{8 \ln 2}{\hat{x}_o^2}\left\{(\Delta\hat{\sigma})^2 + \frac{\hat{\sigma}^2(\Delta x_o)^2}{\hat{x}_o^2}\right\}. \tag{C.28}$$

References:

[a]G.F. Knoll, Radiation Detection and Measurement, (John Wiley & Sons, New York, 1979) pp. 737-379.

[b]W. Zimmermann, Rev. Sci. Instr., 32, 1063 (1961).

[c]P.R. Bevington, Data Reduction and Error Analysis for the Physical Sciences (McGraw-Hill, New York, 1969) pp. 104-108.

EVALUATION OF A $^{90}Sr/^{90}Y$ BETA BEAM FLATTENING FILTER

by

Kevin Dean Stansbury

B.S., Kansas State University, 1982

AN ABSTRACT OF

A MASTER'S THESIS

submitted in partial fulfillment of the
requirements for the degree

MASTER OF SCIENCE

Department of Nuclear Engineering

KANSAS STATE UNIVERSITY

Manhattan, Kansas

1984

ABSTRACT

Experimental work was performed to evaluate a $^{90}Sr/^{90}Y$ beta beam flattening filter composed of polyester discs by measuring energy distributions of the attenuated beta particles with a 10.2 mm BC-400 plastic scintillator based spectrometer. Beta beam flattening filters are designed to provide a uniform absorbed dose rate over a large area and are used in conjunction with "point" beta radiation sources for calibration of instruments in the field of beta dosimetry. Three experimental trials were conducted to determined the influence of the filter and its position on the uniformity of the absorbed dose at the calibration area. The variation of the absorbed dose over the area was estimated on the basis of measured spectral average energies and integral count information and the analysis of measured spectra included comparisons to theoretical $^{90}Sr/^{90}Y$ beta particle energy distributions corrected for absorption losses. These analyses indicated that average beta energy was increased in the presence of the filter and the absorbed dose uniformity was sensitive to filter position. For the optimum geometric configuration investigated, the absorbed dose at a depth of 2.43 mg cm^{-2} was estimated to vary less than ±1.6% over a calibration area 20 cm in diameter.